



# JAMES | Journal of Advances in Modeling Earth Systems\*



#### RESEARCH ARTICLE

10.1029/2025MS005119

#### **Key Points:**

- We present a set of aquaplanet experiments with different sea-surface temperatures and with convectionpermitting resolution in the tropics
- The simulations enable studies on the response of atmospheric phenomena from planetary to convective scales to globally uniform ocean warming
- The Hadley cell, Intertropical Convergence Zone, and tropical precipitation extremes respond nonlinearly to uniform ocean warming

#### Correspondence to:

R. Rios-Berrios, rberrios@ucar.edu

#### Citation

Rios-Berrios, R., Emanuel, K., Bryan, G. H., Medeiros, B., & Done, J. (2025). Response of tropical climate and extreme precipitation to ocean temperature in convection-permitting aquaplanet simulations. *Journal of Advances in Modeling Earth Systems*, 17, e2025MS005119. https://doi.org/10.1029/2025MS005119

Received 28 MAR 2025 Accepted 25 SEP 2025

© 2025 The Author(s). Journal of Advances in Modeling Earth Systems published by Wiley Periodicals LLC on behalf of American Geophysical Union. This is an open access article under the terms of the Creative Commons Attribution-NonCommercial-NoDerivs License, which permits use and distribution in any medium, provided the original work is properly cited, the use is non-commercial and no modifications or adaptations are made.

# Response of Tropical Climate and Extreme Precipitation to Ocean Temperature in Convection-Permitting Aquaplanet Simulations

Rosimar Rios-Berrios<sup>1</sup>, Kerry Emanuel<sup>2</sup>, George H. Bryan<sup>1</sup>, Brian Medeiros<sup>1</sup>, and James Done<sup>1,3</sup>

<sup>1</sup>NSF National Center for Atmospheric Research, Boulder, CO, USA, <sup>2</sup>Lorenz Center, Massachusetts Institute of Technology, Cambridge, MA, USA, <sup>3</sup>Willis Research Network, London, UK

**Abstract** Tropical climate and weather systems are integral to the global hydrological cycle. Yet, their detected and projected trends are highly uncertain in part due to shortcomings of Earth system models. This study uses novel aquaplanet simulations with different sea-surface temperature and with convection-permitting resolution in the tropics to simulate the response of tropical phenomena to globally uniform warming. The results show a complex response within the tropical circulation. With warming, the tropical troposphere warms and expands vertically alongside a weaker and broader Hadley cell. Simultaneously, the Intertropical Convergence Zone (ITCZ) narrows and strengthens, though its location shows an unclear response to warming. Both dynamic and thermodynamic processes play a role in the ITCZ response, exhibiting patterned changes in vertical velocity and magnitude changes in water vapor. Clouds also show a complex response, particularly with tropical cloud ice showing a non-linear response to tropical warming and likely causing non-linear changes in the radiation budget. At finer scales, tropical precipitation extremes increase non-linearly with warming, exceeding Clausius-Clapeyron scaling at higher percentiles. The prevalence of non-linear responses highlights the necessity of considering multiple scenarios when investigating the response of tropical phenomena to globally uniform warming. This research provides valuable insights into tropical climate sensitivity in a framework that captures multi-scale processes from global to convective scales.

Plain Language Summary As our planet warms, weather patterns worldwide may also shift in frequency and intensity. However, predicting the specifics of these changes is challenging, especially in the tropical atmosphere where towering clouds and heavy rain are essential parts of weather systems. A key reason for this uncertainty is that current climate models struggle to accurately represent these towering clouds and heavy rainfall, overlooking crucial rainfall-producing features in the tropics. In this study, we utilize innovative model simulations that capture these fine details in the tropics while also representing the global climate. We present three simulations that differ only in their ocean temperature—one simulation mimics our current climate, while the other two simulate cooler and warmer climates. Our findings highlight the importance of capturing small-scale tropical processes, as the climate exhibits various responses to uniform warming. Tropical weather systems generate more intense extreme rainfall, likely connected to changes in the overall tropical environment. Future research should leverage these simulations to explore how specific weather systems, such as tropical cyclones, evolve in a warmer climate.

# 1. Introduction

There are many uncertainties about how tropical climate and weather will change as the global climate changes. Climate projections disagree on key aspects of the intertropical convergence zone (ITCZ), such as whether it will expand or contract, intensify or weaken, shift location, or remain in place (Byrne et al., 2018). There is similar uncertainty about projected changes in tropical weather systems; for instance, studies show conflicting results on whether the frequency of tropical cyclones will increase or decrease (Knutson et al., 2020), and whether convectively coupled Kelvin waves will strengthen or weaken under global warming (Bartana et al., 2022). Examining potential changes in tropical weather systems in a changing climate requires a modeling framework that can capture both global and convective scales. Current studies are limited to either comprehensive climate simulations with long integration times but coarse resolution, or convection-permitting simulations with high enough resolution to resolve deep convection but limited to specific regions or single case studies. This study aims

RIOS-BERRIOS ET AL. 1 of 25

to bridge the gap between those approaches by examining the response of tropical climate and rainfall to ocean warming in idealized global simulations with convection-permitting resolution in the tropics.

The tropics play a crucial role in Earth's climate system, prompting extensive research into observed and projected changes in large-scale tropical circulation. The Hadley cell and its ascending branch (the ITCZ) have been of particular interest, with a focus on changes in both width and strength (see reviews by Birner et al., 2014; Lionello et al., 2024; Lucas et al., 2013; Seidel et al., 2007; Staten et al., 2018, 2020). Observations and historical simulations concur that the Hadley cell has been expanding since the start of the satellite era (Hu & Fu, 2007; J. Lu et al., 2007), and most models from the last two Coupled Model Intercomparison Project iterations (CMIP5 and CMIP6) predict this trend to continue (Xia et al., 2020). There is also agreement about a projected weakening Hadley cell in a future warmer climate (Xia et al., 2020). However, reanalysis and historical climate models show differing trends in Hadley cell strength. Reanalysis data sets, used as proxies for observations, show that the Hadley cell has been *strengthening*, whereas climate models show a *weakening* Hadley cell during the same historical period (e.g., Chemke & Yuval, 2023; Lionello et al., 2024). This discrepancy arises from differences in the thermodynamic structure from reanalysis and climate models (Mitas & Clement, 2006), which leads to uncertainty about which data set is more reliable.

On the other hand, studies about ITCZ changes amid a changing climate have focused on its location, strength, and width. Byrne et al. (2018) reviewed current knowledge on each of those ITCZ properties, which can be summarized as follows. Observations during the historical record show that the ITCZ has changed little in position whereas it has been narrowing and strengthening over the past decades. Climate projections show a wide range of potential changes in ITCZ location, with multi-model means showing negligible changes in this metric. Most CMIP5 models predict a narrowing and weakening ITCZ (Byrne et al., 2018, their Figure 3). An examination of physical mechanisms responsible for the ITCZ narrowing exposed an interplay between the time mean circulation, net energy input, and transient eddies, and such interplay varied considerably between models (Byrne & Schneider, 2016). These uncertainties in historical and future projections of the large-scale tropical circulation can lead to uncertainties of the future tropical hydrological cycle and, more specifically, on weather events that are sensitive to the state of large-scale conditions.

In a related manner, changes in extreme tropical rainfall are more sensitive to global warming and harder to predict than extreme precipitation in other regions (O'Gorman, 2012; O'Gorman & Schneider, 2009a). Observations show that tropical precipitation extremes (defined as a high percentile from a distribution) have increased by an average of  $9\%~K^{-1}$ , whereas in the extratropics the average observed increase is  $4\%~K^{-1}$  (Asadieh & Krakauer, 2015; O'Gorman, 2015). Uncertainty in these estimates is greater in the tropics, partly due to the sparse availability of in situ observations (Westra et al., 2013). Most comprehensive Earth system models project that precipitation extremes will continue to intensify, with projected rates varying between 7% and  $15\%~K^{-1}$  in the tropics and  $6\%-7\%~K^{-1}$  in the extratropics (O'Gorman, 2015, their Figure 2). Thus, observed and projected changes in extreme tropical precipitation are both stronger and more uncertain than in the extratropics.

Uncertainties in future climate projections are partly due to limitations in climate models. The coarse resolution of these models necessitates the use of convection parameterizations to represent deep convection, but precipitation extremes can vary significantly depending on the specific parameterization (e.g., Wilcox & Donner, 2007). These models struggle to accurately represent mesoscale-to-synoptic scale weather phenomena. For example, these models also cannot physically represent mesoscale convective systems (Moncrieff, 2019; Moncrieff & Liu, 2006), which contribute over half of the annual precipitation in the tropics (Feng et al., 2021; Nesbitt et al., 2006). The inability to represent these systems means that climate models are missing crucial rainfall-producing weather features in the tropics (Rossow et al., 2013).

Convection-permitting models can reduce some of the aforementioned uncertainties. These models use small enough grid spacing to explicitly resolve deep convection and convective systems (hence why they are also called "storm-resolving" models; Stevens et al., 2019). Changes in precipitation can be directly linked to the modeled state variables due to explicitly resolved processes (Muller et al., 2011), and tropical weather systems are represented with better fidelity (Judt & Rios-Berrios, 2021; Rios-Berrios, Judt, et al., 2023). Although these models are too computationally expensive to be integrated on the globe for many decades, studies have already shown the value of year-long convection-permitting global simulations. For example, some studies have compared simulations with present sea-surface temperature (SST) and with either SST or CO<sub>2</sub> levels increased to mimic a future

RIOS-BERRIOS ET AL. 2 of 25

19422466, 2025, 10, Downloaded from https://agupubs.onlinelibrary.wiley.com/doi/10.1029/2025MS005119 by Kerry Emanuel , Wiley Online Library on [26/10/2025]. See the Term

**Figure 1.** Snapshot of outgoing longwave radiation from an aquaplanet simulation analyzed in this study. The global map depicts the entire domain, whereas the three boxes at the bottom show zoomed in snapshots of (from left to right): a tropical cyclone, a squall line, and a mesoscale convective system.

climate, finding that their modeled response generally falls within the spread of CMIP-type simulations (Bao et al., 2024; Merlis et al., 2024; Terai et al., 2025). Whether these short simulations produce robust results compared to long climate change experiments is unknown, as multi-year coupled simulations are only beginning to be conducted (Rackow et al., 2025; Segura et al., 2025).

These limitations motivate this study, which aims at investigating changes in the tropical climate and extreme precipitation in a global modeling framework that captures convective-scale dynamics (Figure 1). We use an aquaplanet framework, which is an idealized representation of Earth without heterogeneity associated with land, sea-ice, and seasons. The aquaplanet framework is driven by zonally symmetric and meridionally varying seasurface conditions that mimic Earth's surface. We investigate the sensitivity of tropical climate and weather to ocean warming by uniformly decreasing or increasing the SST by 4 K. The latter is one of several methods used by the Cloud Feedback Model Intercomparison Project (Webb et al., 2017) to isolate changes in the general circulation due to surface warming. While warming oceans is only one of many components of climate change, this method allows us to isolate the sensitivity of tropical climate and rainfall to globally uniform ocean warming and its associated atmospheric response.

Moreover, we employ convection-permitting resolution in the tropics to capture the convective-scale dynamics of tropical weather systems. The underlying SST profile peaks in the Northern Hemisphere to enable tropical cyclone activity. Although other studies have already used convection-permitting aquaplanets with SSTs increased by 4 K (e.g., O'Gorman et al., 2021), their SST profiles typically peaked at the equator and did not support tropical cyclone formation. Our configuration is—to our knowledge—the first of its kind in studies of climate and rainfall changes in a warming world. Figure 1 shows a snapshot of one of our simulations. Key elements of the tropical atmosphere are evident, including the ITCZ, tropical cyclones, mesoscale convective systems, and squall lines. This configuration bridges a gap between global and limited-area modeling by using a single experimental setup to comprehensively study changes in tropical phenomena all the way from global to convective scales.

The objectives of this paper are twofold. We seek to document the model simulations while also discussing their simulated changes in the tropical climate and changes in tropical rainfall extremes. We describe the model simulations in Section 2. We discuss the atmospheric response to a globally uniform warming in Section 3. We take a "telescopic" approach by first focusing on the global climate, and them zooming into the tropical climate

RIOS-BERRIOS ET AL. 3 of 25

19422466, 2025, 10, Downloaded from https://agupubs.onlinelibrary.wiley.com/doi/10.1029/2025MS005119 by Kerry Emanuel , Wiley Online Library on [26/10/2025]. See the Terms and Cor

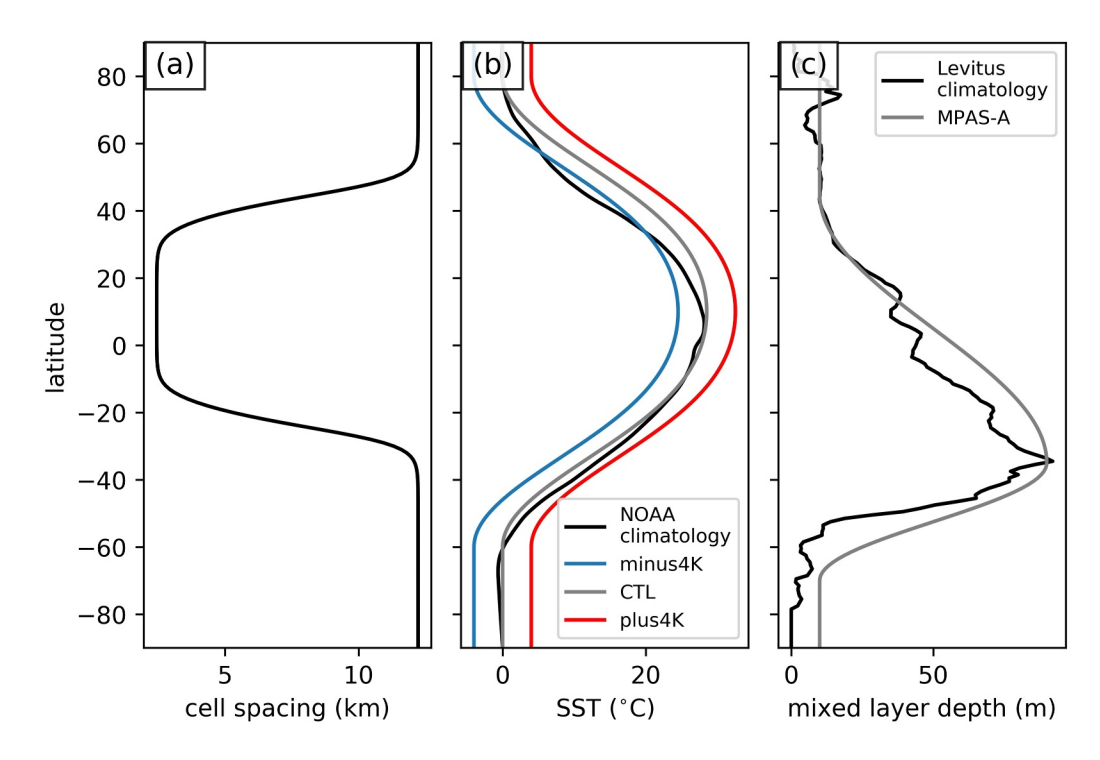


**Figure 2.** Latitudinal profiles of (a) horizontal cell spacing, (b) sea-surface temperature (SST), and (c) ocean mixed layer depth. In panel (b), the black line represents the 1981–2020 June–September mean zonally averaged SST, whereas the blue, gray, and red lines represent the minus4K, CTL, and plus4K experiments, respectively. In panel (c), the black line represents the time mean, zonal mean ocean mixed layer depth from Levitus (1982), whereas the gray line represents an analytical approximation used in all MPAS-A experiments.

and tropical precipitation extremes. We link our results to detected and projected changes whenever possible. Lastly, we present a summary and discussion in Section 4.

#### 2. Methods

#### 2.1. Experimental Setup

We produced a set of idealized experiments using the Model for Prediction Across Scales-Atmosphere (MPAS-A) (Skamarock et al., 2012) version 8.0. MPAS-A is a community model that enables both global and regional simulations of the atmosphere. The model grid uses an Arakawa-C discretization on a Voronoi tessalation, which allows for both uniform and variable horizontal grid resolution. Our experiments use an aquaplanet configuration as an idealized representation of Earth's climate system, which removes uncertainties due to land-atmosphere interactions, continental boundaries, seasonal changes, etc. Previous studies have demonstrated that MPAS-A aquaplanet experiments produce results consistent with aquaplanet configurations in other general circulation models, especially in the tropics (Rios-Berrios et al., 2020, 2022, 2024; Rios-Berrios, Davis, & Martinez, 2023; Rios-Berrios, Judt, et al., 2023).

Our aquaplanet configuration is similar to that of Rios-Berrios, Judt, et al. (2023), with some important differences. The model was configured as a water-covered sphere without land or sea-ice. Given our interest in tropical weather systems, we employed a variable-resolution domain with approximately 3 km horizontal cell spacing between 10°S–30°N (Figure 2a). The horizontal cell spacing transitioned to approximately 12.3 km by 30°S and 55°N. The smallest cell spacing coincided with the region of warmest SSTs in all experiments, although precise SST varied by experiment. The model time step was specified as 15 s to maintain model stability. A 3-km horizontal mixing length was used for the horizontal diffusion, which used the Smagorinsky (1963) formulation. The vertical grid consisted of 70 vertical levels with grid spacing stretching from ~50 m near the surface to ~640 m by the model top at 30 km. A gravity-wave absorbing layer above 22 km applied Rayleigh damping to the vertical velocity following Klemp et al. (2008). These computational settings were chosen from available options in MPAS-A.

RIOS-BERRIOS ET AL. 4 of 25

Our control experiment (CTL hereafter) used the same SST profile as in Rios-Berrios, Judt, et al. (2023) and originally introduced by Ballinger et al. (2015). This profile is intended to mimic boreal summer surface conditions and is given by:

$$SST(\phi) = \begin{cases} SST_0 \left\{ 1 - \frac{1}{2} \left[ sin^2 \left( \frac{\phi - \phi_0}{140} \pi \right) + sin^4 \left( \frac{\phi - \phi_0}{140} \pi \right) \right] \right\}, & \phi_0 - 70^\circ < \phi < \phi_0 + 70^\circ \\ 0, & \text{elsewhere} \end{cases}$$
 (1)

where  $\phi$  is latitude,  $\phi_0$  is the latitude of maximum SST (set as 10°N), and  $SST_0$  is the maximum SST (set as 28.5°C). Figure 2b shows this profile, which mimics the climatological June-September SST of the Pacific Ocean. This is demonstrated by the time mean, zonal mean SST obtained from the NOAA Optimum Interpolation data set averaged over the Pacific Ocean from 1981 to 2020 (Huang et al., 2021). Two other experiments were performed to uniformly increase or decrease the SST by 4 K at all cells. These experiments will be called "plus4K" and "minus4K," respectively, hereafter. A caveat of this approach is that a uniform SST change results in a non-uniform change in saturation moist entropy due to the non-linear dependence of saturation specific humidity on temperature, thus imposing differing equator-to-pole saturation moist entropy gradients across experiments. In a moist convecting atmosphere, atmospheric circulations are more nearly driven by gradients of sea surface saturation moist entropy than by SST gradients (Emanuel et al., 1994). This must be considered when interpreting how the global climate responds to ocean warming. All simulations used the same CO<sub>2</sub> concentration.

Another key distinction between this study and previous MPAS-A aquaplanet studies is the treatment of surface heat fluxes and surface temperature. We added dissipative heating to the YSU planetary-boundary layer scheme and updated the wind-speed dependent parameterization of roughness length to match more closely the revised estimates of Curcic and Haus (2020). Additionally, we incorporated a 1-D ocean mixed layer depth model (Pollard et al., 1973) to allow the SST to respond locally to tropical cyclones and squall lines. Specifically, this model calculates the mixed layer depth (h) based on wind stress, a prescribed lapse rate of the water temperature within the mixed layer, and the surface heat and radiative fluxes. The SST responds to changes in h and then relaxes back to its initial value over a time period  $\tau$ . The base-state mixed layer depth was prescribed as a fit to time mean, zonal mean data from Levitus (1982), given by

$$h(\phi) = 10 + \begin{cases} h_m \left[ 1 - \sin^2 \left( \frac{(\phi - \phi_m)\pi}{160} \right) \right], & \phi_0 < \phi < \phi_m + 80^\circ \\ h_m \left[ 1 - \sin^2 \left( \frac{(\phi - \phi_m)\pi}{70} \right) \right], & \text{elsewhere} \end{cases}$$
 (2)

where  $h_m$  is the maximum base-state mixed layer depth (set as 80 m) and  $\phi_m$  is the latitude of  $h_m$  (set as 35°S). Figure 2c shows both the time mean, zonal mean profile (over June-September) and the prescribed ocean mixed layer depth. Both exhibit strong latitudinal variations with the shallowest layers in the Northern Hemisphere and the deepest layers in the Southern Hemisphere, coinciding with the latitude of maximum midlatitude cyclone activity. All experiments used the same ocean mixed layer depth to avoid introducing differences between the experiments other than the underlying SST. A small value of  $\tau$  (5 days) was used to avoid a climatological drifting of the prescribed SST profile while also capturing ocean cooling due to high-wind events. Importantly, this approach considers only transient events and does not impose a cross-equatorial ocean heat flux.

Given our interest in simulated weather phenomena at convection-permitting resolution, we utilized physics packages rigorously tested by the numerical weather prediction community. We used Thompson microphysics (Thompson et al., 2008), together with the Thompson scheme for estimating sub-grid-scale cloud fraction, to incorporate the advantages of double-moment microphysics (Bryan & Morrison, 2012; Igel et al., 2015; Morrison et al., 2009). We also used updated versions of the YSU (Hong et al., 2004) and scale-aware Tiedtke schemes (Wang, 2022) that were available in MPAS-A v8.0. Lastly, all simulations employed the RRTMG scheme (Iacono et al., 2008; Mlawer et al., 1997) for both shortwave and longwave radiation with perpetual equinoctial conditions given by a fixed declination angle (0°), fixed solar constant (1,365 W m<sup>-2</sup>), radiatively inactive aerosols, and a hemispheric symmetric ozone profile.

RIOS-BERRIOS ET AL. 5 of 25

All three simulations were integrated for 240 days (approximately 8 months). The first 60 days were considered spinup; therefore, all analyses presented here are limited to the last 180 days (approximately 6 months). We recognize that this integration period is relatively short in comparison to the multi-year period typically used for aquaplanet experiments. However, these simulations cost approximately 50,000 CPU core-hours per day and produced 400 GB data per day totaling 36 Million CPU core-hours and nearly 300 TB of raw model output in the Derecho supercomputing system (Computational and Information Systems Laboratory, 2023). These high computational costs and storage demands prevent us from producing multi-year simulations at this point. Nonetheless, evaluation of several globally-averaged metrics showed that the simulations reached near equilibrium by 30 days (not shown). The integration period is sufficient to demonstrate the potential response of the atmosphere to ocean warming and to examine the statistics of weather phenomena in a convection-permitting configuration.

#### 2.2. Model Output Interpolation

Our examination of the global and tropical climate (Sections 3.1 and 3.2) used model output interpolated to a  $1^{\circ} \times 1^{\circ}$  latitude-longitude global grid given our focus on the planetary-scale response. Additionally, we used model output interpolated to a  $0.25^{\circ} \times 0.25^{\circ}$  latitude-longitude in Section 3.3. We used the Climate Data Operators (Schulzweida, 2022) tool with conservative interpolation from the native 15-3 km MPAS-A mesh to the latitude-longitude fixed grids. Conservative interpolation ensures that the global sum of each quantity is conserved during interpolation. The interpolated model output is publicly available for future studies (Rios-Berrios, 2025a). We used the native model output for a select number of diagnoses in this study, and we mention when we did so in the appropriate section.

#### 3. Results

#### 3.1. Global Climate

As expected, the simulated climate responds in various ways to the prescribed SSTs. We illustrate this response via cross-sections of time mean, zonal mean differences between CTL and minus4K and between plus4K and CTL (Figures 3 and 4). Notably, the troposphere warms at all latitudes (Figures 3a and 3b). The tropopause level, diagnosed from the potential temperature lapse rate following Tinney et al. (2022), moves upward with height at nearly all latitudes. The 0°C level also moves higher with warmer temperatures (lifting the melting level, as will be discussed below). Peak tropospheric warming happens in the upper tropical troposphere, where differences between experiments reach up to 11 K. This large warming exceeds the 4 K SST difference between each consecutive experiment, which implies a combined effect of increased ocean temperatures, saturation moist entropy, and free-tropospheric moist entropy (Emanuel et al., 1994).

The polar stratosphere cools with warming, intensifying the isobaric temperature difference between the tropics and the poles. Simultaneously, the upper-tropospheric westerly jet cores strengthen with warming (Figures 3c and 3d). Such strengthening is evident in both hemispheres as illustrated by positive zonal wind differences of at least 10 m s<sup>-1</sup> at the jet cores around 30°S and 20–30°N. The positive differences are co-located with the Southern Hemisphere jets, but they are shifted equatorward of the Northern Hemisphere jets. This result implies that the summer upper-tropospheric jet strengthens *and* shifts slightly equatorward with globally uniform warming in our simulations.

As the troposphere warms, it holds an increasing amount of water vapor. However, the saturated vapor pressure increases more rapidly at a constant relative humidity, leading to a larger saturation deficit. This increase in saturation deficit with warming is evidenced by positive differences in saturation deficit at almost all latitudes (Figures 4a and 4b). The pattern of differences between experiments largely coincides with the overall structure of saturation deficit (as represented by CTL in black contours; Figures 4a and 4b). The largest differences between experiments appear in the Southern Hemisphere subtropics, where saturation deficit is the largest. The Northern Hemisphere subtropics and middle latitudes are also associated with drier conditions as the ocean warms. The smallest, yet positive, differences appear within a narrow band in the tropics—this coincides with the ITCZ (as will be discussed below).

Using convection-permitting resolution in the tropics allows us to investigate changes in condensate as simulated by the microphysics scheme and the model equations. Total condensate (the sum of all liquid and frozen water

RIOS-BERRIOS ET AL. 6 of 25

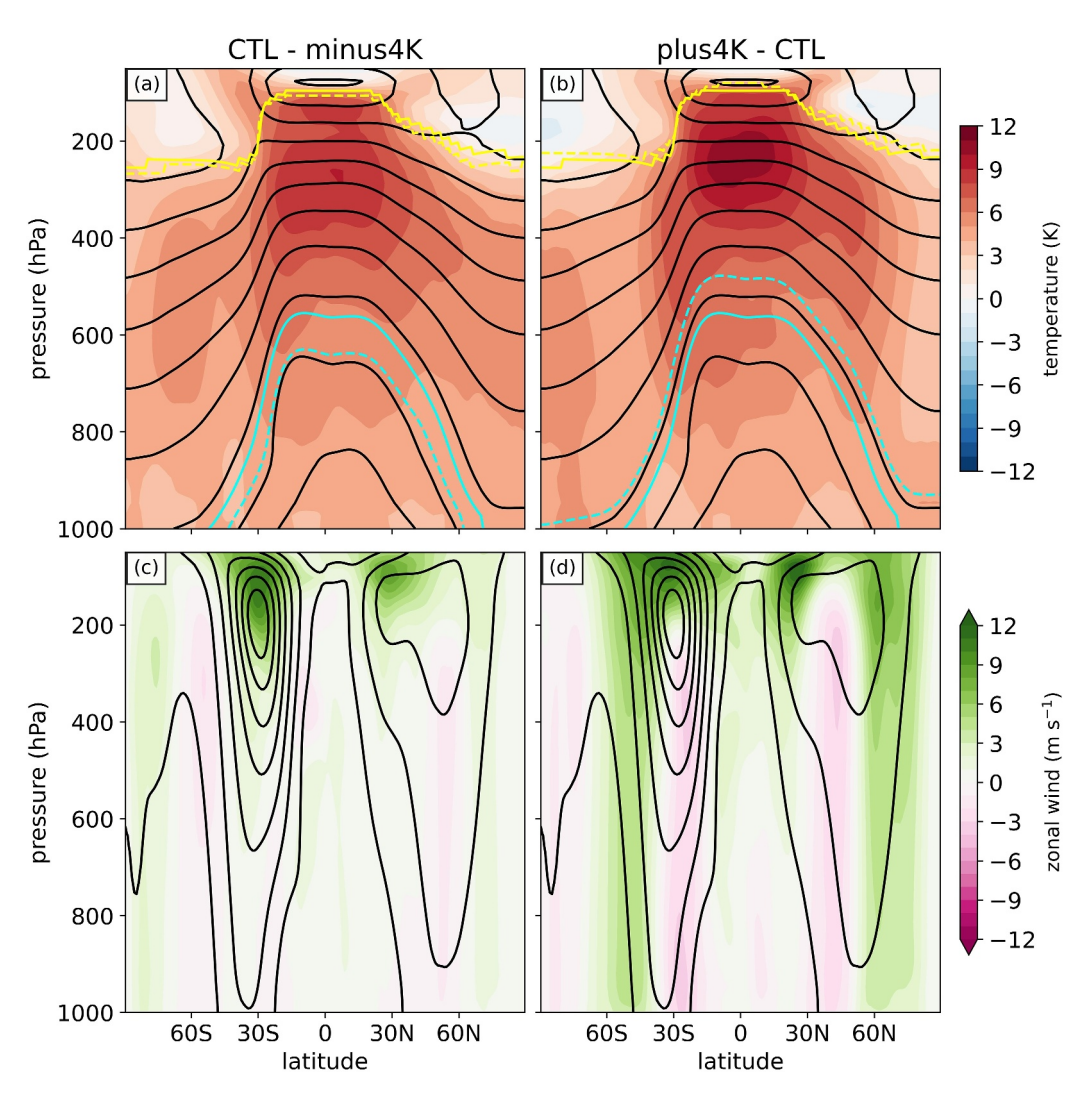


**Figure 3.** Pressure-latitude analyses of the differences between (a, c) CTL and minus4K and (b, d) plus4K and CTL. Color shading represents the time mean, zonal mean difference of (a, b) temperature (every 1 K) and (c, d) zonal wind (every 1 m s<sup>-1</sup>). Black contours in all panels represent the time mean, zonal mean from CTL. In panels (a)–(b), the cyan lines show the 0°C temperature and the yellow lines show the tropopause level from CTL (solid) and either minus4K (dashed; panel a) or plus4K (dashed; panel b).

content) exhibits peculiar changes with warming (Figures 4c and 4d). Consistent with the expanding tropical troposphere, the overall amount of upper-tropospheric condensate in the tropics increases in amount and height above 600 hPa from minus4K to CTL and above 500 hPa from CTL to plus4K. This change indicates that frozen condensate in the tropics increases and extends over a deeper layer with warming. Likewise, liquid condensate in the tropics increases with warming below 700 hPa from minus4K to CTL and below 600 hPa from CTL to plus4K.

However, the total condensate in the tropics decreases with warming within a layer between 600 and 700 hPa from CTL to minus4K and between 500 and 600 hPa from plus4K to CTL. This layer corresponds to the increasing height of the melting level, as measured by the 0°C wet-bulb temperature (cyan lines in Figures 4c and 4d). The tropical melting level shifts from ~675 hPa in minus4K to ~600 hPa and ~500 hPa in CTL and plus4K, respectively. As the melting level rises, snow and graupel melt at a higher altitude. The resulting conversion to raindrops, which have larger fall velocity, leads to a decrease in total condensate below the melting level. This upward shift with warming can alter other microphysical processes, potentially increasing local surface rainfall. For example, Prein and Heymsfield (2020) showed that the observed melting level has increased in unison with rising surface temperatures on Earth. They argue that the increasing melting level height enhances surface

RIOS-BERRIOS ET AL. 7 of 25

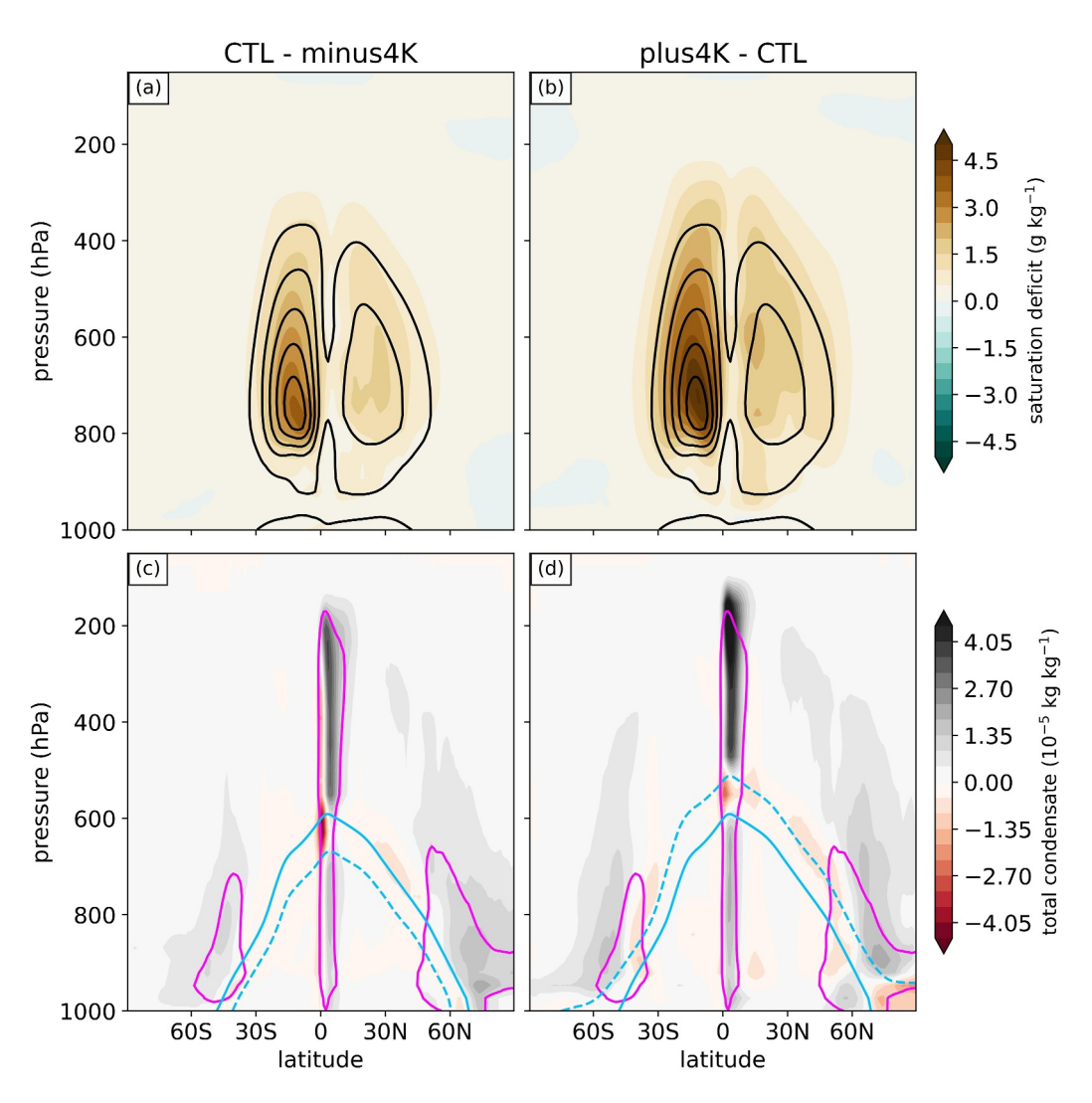


**Figure 4.** As in Figure 3, except for (a, b) saturation deficit (every 0.5 g kg<sup>-1</sup>) and (c, d) total condensate (every 0.45 kg kg<sup>-1</sup>). In panels (c)–(d), the magenta lines represent the time mean, zonal mean total condensate from CTL, and the cyan lines show the 0°C wet bulb temperature from CTL (solid) and either minus4K (dashed; panel c) or plus4K (dashed; panel d).

precipitation by enabling more graupel to melt over a deeper layer and by increasing the vertical extent through which raindrops can form and grow.

In a related manner, our simulations show increasing rainfall rates with globally uniform warming, especially in the tropics. This result is shown in Figure 5a through the time mean, zonal mean rainfall rates. A tropical peak marks the ITCZ, whereas secondary peaks mark the midlatitude storm tracks. The maximum time mean, zonal mean rainfall rate increases from 18.0 mm day $^{-1}$  in minus4K to 18.8 mm day $^{-1}$  in CTL and 24.8 mm day $^{-1}$  in plus4K (Table 1). These changes yield only  $\sim 1\%$  K $^{-1}$  change from minus4K to CTL but  $\sim 7\%$  K $^{-1}$  change from CTL to plus4K, which is close to the Clausius-Clapeyron scaling. There is also a slight increase in rainfall rates around 30°N, which is likely associated with tropical cyclones. Midlatitude rainfall rates (around 30°S–60°S and poleward of 60°N) increase in magnitude and shift poleward with warming. This result suggests that the storm tracks move poleward with warming in these aquaplanet simulations.

When evaluated on a global scale, ocean warming results in an increase in time mean, global mean precipitation. We obtained this quantity using model output at its native resolution, weighted by the area of each cell, and time averaged over the 180 days of analysis. Global rainfall rates are 3.16 mm day<sup>-1</sup>, 3.64 mm day<sup>-1</sup>, and 4.13 mm day<sup>-1</sup> in minus4K, CTL, and plus4K, respectively (Table 1). The equivalent rate of change is 3.8% K<sup>-1</sup> from

RIOS-BERRIOS ET AL. 8 of 25

1942-2466, 2025, 10, Downbaded from https://agupubs.onlinelibrary.wiley.com/doi/10.1029/2025MS005119 by Kerry Enanuel, Wiley Online Library on [26/10/2025]. See the Terms and Conditions (https://onlinelibrary.wiley.com/

and-conditions) on Wiley Online Library for rules of

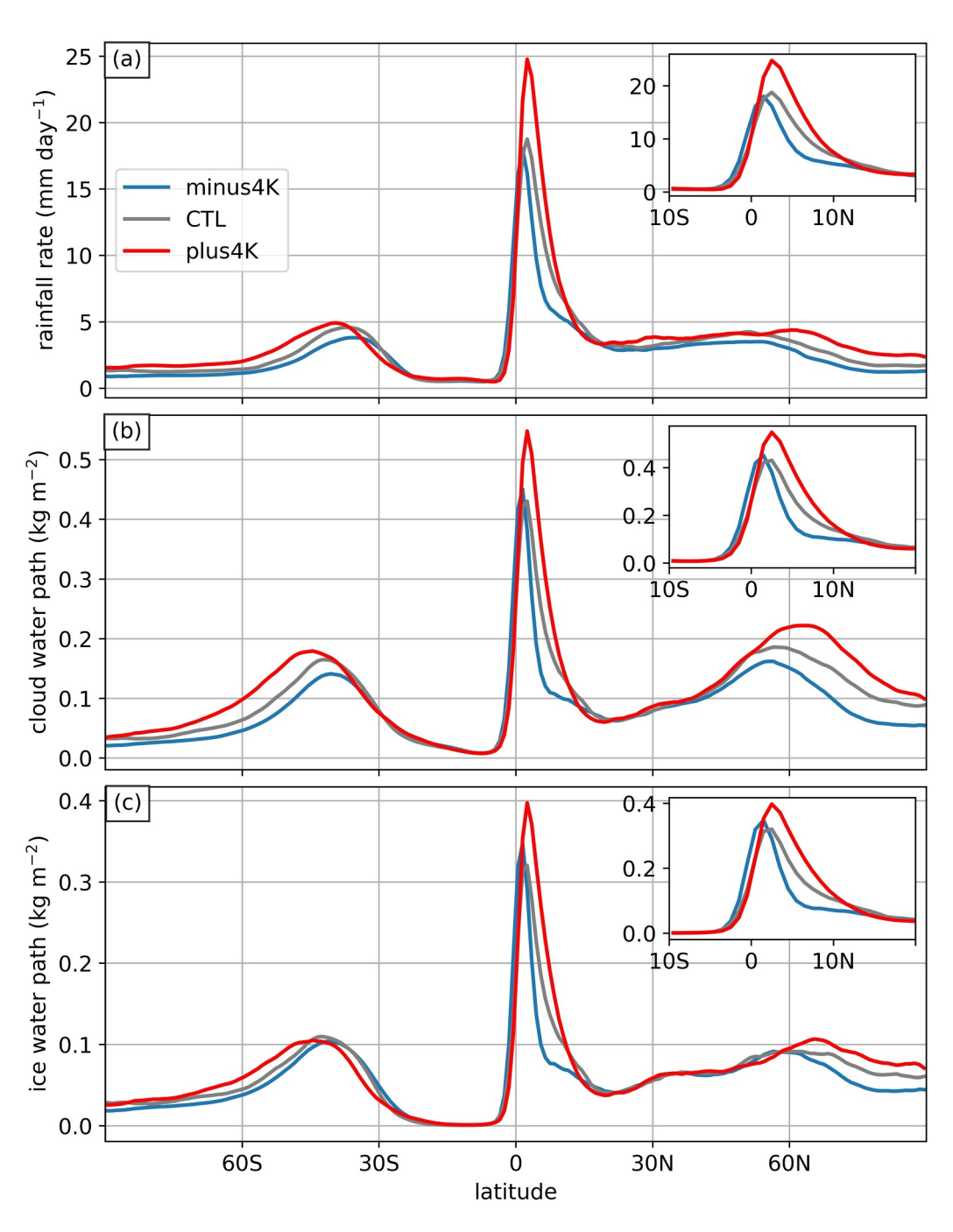


Figure 5. Time mean, zonal mean (a) rainfall rate, (b) cloud (liquid + ice) water path, and (c) cloud ice water path from (blue) minus4K, (gray) CTL, and (red) plus4K. The insets show each variable zoomed in to the tropics.

minus $^4$ K to CTL and  $^3.4\%$  K $^{-1}$  from CTL to plus $^4$ K. These rates are below Clausius-Clapeyron scaling due to compensating radiative cooling and latent heating (Held & Soden,  $^2$ 006; Muller & O'Gorman,  $^2$ 011). The increased global rainfall rates are predominantly contributed by increased rainfall in the tropics, as noted above.

Despite the robust increasing signal of rainfall rates, clouds show a more complex response to warming. This result is shown in Figure 5b through the time mean, zonal mean cloud water path. Unlike total condensate, the cloud water path only includes cloud water, cloud ice, and snow as they are all treated as "clouds" in the Thompson cloud fraction scheme. Rain and graupel are excluded from this calculation. Although there is an overall increase in cloudiness with globally uniform warming, peak values within the ITCZ slightly decrease from

RIOS-BERRIOS ET AL. 9 of 25

**Table 1** (Left to Right) Maximum Time Mean, Zonal Mean Rainfall Rate ( $pr_{max}$  in mm  $day^{-1}$ ) and Time Mean, Global Mean Rainfall Rate ([pr]; in mm  $day^{-1}$ ) in the Experiments Considered in This Study

Experiment	$pr_{\text{max}}$	[pr]
minus4K	18.0	3.16
CTL	18.8	3.64
plus4K	24.8	4.13

minus4K to CTL, whereas they increase between plus4K and CTL (Figure 5b). The slight decrease between minus4K and CTL is mostly contributed by decreasing ice clouds between this pair of experiments as demonstrated by the cloud ice water path (Figure 5c). There is a reduction of ice clouds within the ITCZ from minus4K to CTL, but an increase in ice clouds from CTL to plus4K; otherwise, there is a general increase of ice clouds with warming. Since peak rainfall rates increase by 3.4% K<sup>-1</sup> from minus4K to CTL, the reduction in cloud ice is likely compensated by increasing in liquid water content between those two experiments. This result points at shifting microphysical processes with warming.

Outside the tropics, total condensate decreases in the subtropics and it primarily increases in the midlatitudes with uniform warming. This is evident in both the vertical cross sections of total condensates (Figures 4c and 4d) and the cloud water paths (Figures 5b and 5c). Decreasing condensate in the subtropics is likely a result of the greater saturation deficit with warming, while the increasing condensate in the midlatitudes is likely due to strengthening midlatitude storms. These issues will not be investigated further in this study due to our focus on tropical climate.

Changes in cloud properties have significant potential to alter the Earth's radiation budget. This is underscored by numerous studies highlighting that uncertainties in how climate models represent clouds and their interactions with radiation are major sources of disagreement in future climate projections (Bony & Dufresne, 2005; Cess et al., 1990; Dufresne & Bony, 2008; Medeiros et al., 2008; Sherwood et al., 2014; Webb et al., 2012). Consistent with this understanding, our simulations reveal variations in the top-of-atmosphere (TOA) radiation budget (Figure 6). Specifically, we observe a general reduction in outgoing shortwave radiation with globally uniform warming across most latitudes, with a notable exception between 15°N and 20°N (Figure 6a). Within this specific latitudinal band, the plus4K simulation stands out with a substantially larger TOA shortwave radiative flux. Notably, this simulation also exhibits the lowest amount of column-integrated cloud within the 15°N–20°N region (Figure 5b), suggesting a potential link between reduced cloud cover and the increased shortwave radiation. Conversely, outgoing longwave radiation (radiative cooling) increases with surface warming across all our simulations (Figure 6b). The combined effect of these shortwave and longwave changes results in an increased net TOA radiative cooling poleward of  $\pm 30^{\circ}$  and less warming within those latitudes (Figure 6c). However, the 15°N-20°N region remains an exception, where the higher outgoing shortwave flux in the plus4K experiment leads to a higher net TOA radiative flux compared to other simulations. Understanding the underlying cloud feedbacks responsible for this unique behavior in the 15°N-20°N region requires further in-depth analysis, which will be left for a future study.

The global mean TOA radiative fluxes can be used to characterize the climate sensitivity in these experiments, similar to the classic approach of Cess et al. (1990), and following conventions of Merlis et al. (2024). A total feedback parameter is calculated as

$$\lambda = \frac{\Delta N}{\Delta T_s},$$

$$\frac{F_{CO_2}}{\lambda}$$

resulting in a climate sensitivity of  $1.6 \, \text{K}$  for the warm experiment and  $1.0 \, \text{K}$  for the cool experiment. These values are strongly influenced by cloud feedbacks; the global average values of shortwave cloud-radiative effect hint at a strong negative cloud feedback in the cool experiment that nearly vanishes in the warm experiment (-65.94, -72.15, and  $-72.18 \, \text{W} \, \text{m}^{-2}$  in minus4K, CTL, and plus4K, respectively). The global mean shortwave cloud-radiative effect values are much stronger than the observed Earth values (around  $-46 \, \text{W} \, \text{m}^{-2}$ , Loeb

RIOS-BERRIOS ET AL. 10 of 25

19422466, 2025, 10, Downloaded from https://agupubs.onlinelibrary.wiley.com/doi/10.1029/2025MS005119 by Kerry Emanuel , Wiley Online Library on [26/10/2025]. See the Terms and Conditions (https://onlinelibrary.wiley.

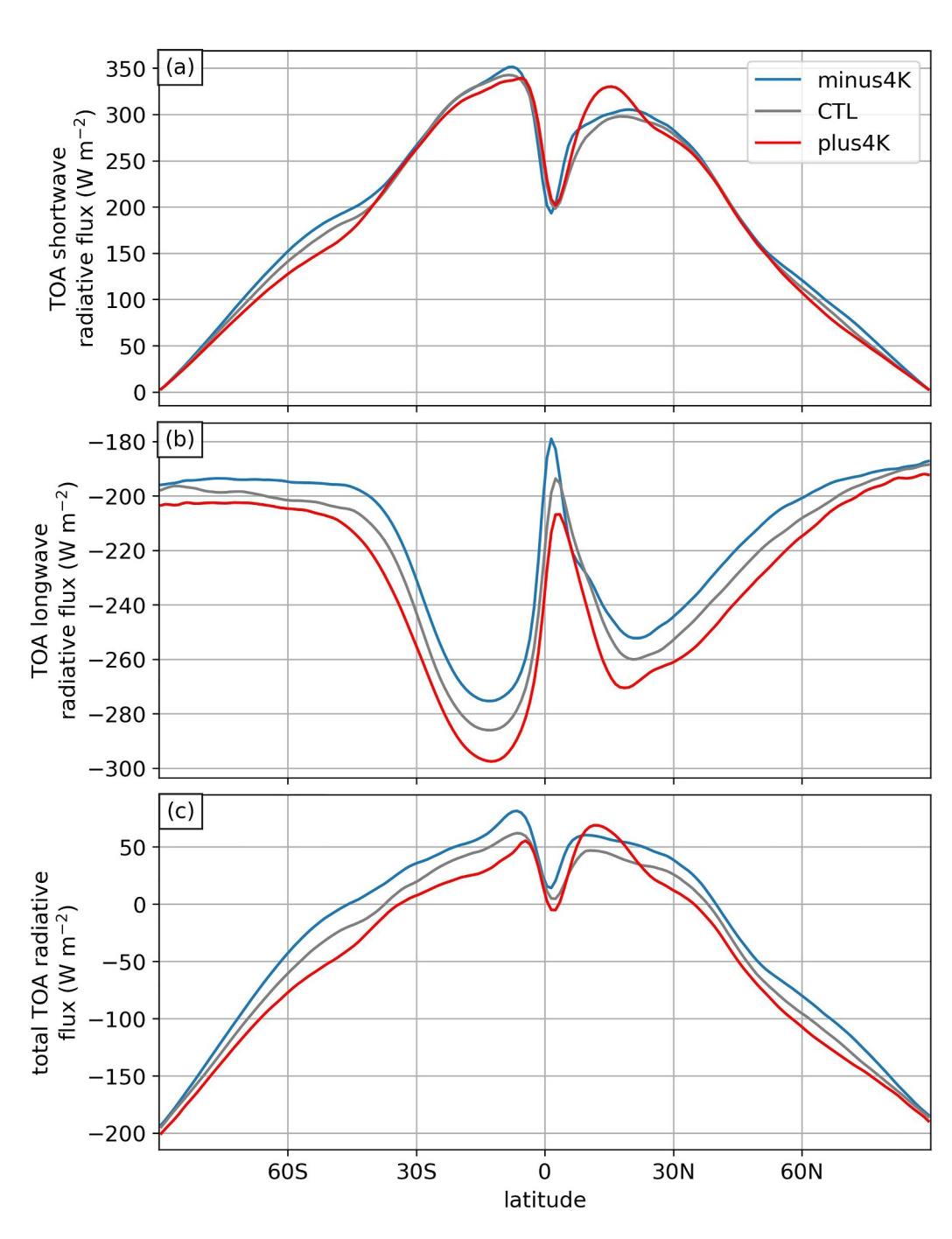


**Figure 6.** Time mean, zonal mean top-of-atmosphere (a) shortwave, (b) longwave, and (c) total radiation fluxes from minus4K (blue), CTL (gray), and plus4K (red).

et al., 2018), but the longwave cloud-radiative effect values are fairly close to Earth values and also show nonlinear behavior across simulations (27.74, 28.39, and 28.02 W  $m^{-2}$ , compared to observed values around 28 W  $m^{-2}$ ).

## 3.2. Tropical Climate

We now turn our attention to changes in the tropical atmosphere, where the Hadley cell and ITCZ exhibit important changes with warming. All simulations develop Hadley cells characterized by moist tropical ascent in

RIOS-BERRIOS ET AL.

19422466, 2025, 10, Downloaded from https://agupubs.onlinelibrary.wiley.com/doi/10.1029/2025M\$005119 by Kerry Emanuel , Wiley Online Library on [26/10/2025]. See

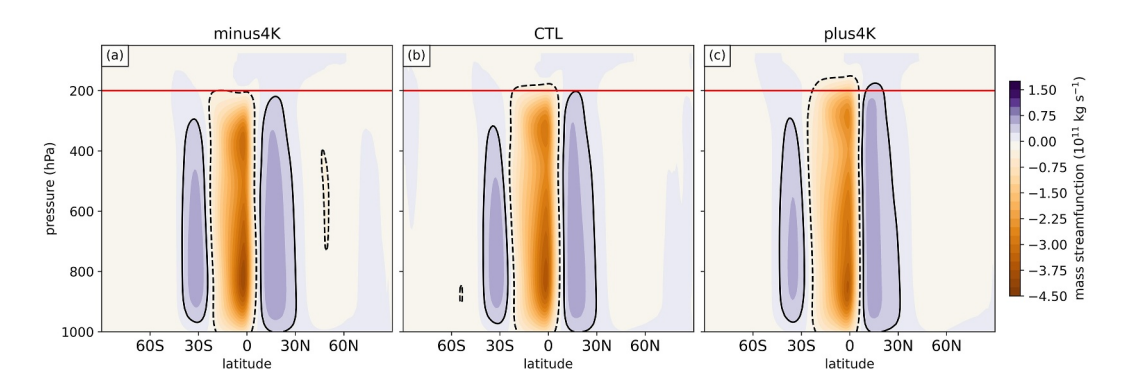


**Figure 7.** Pressure-latitude analysis of the meridional mass streamfunction from (a) minus4K, (b) CTL, and (c) plus4K. Solid and dashed lines represent the  $0.25 \times 10^{11}$  kg s<sup>-1</sup> and  $-0.25 \times 10^{11}$  kg s<sup>-1</sup> contours, respectively. Red lines mark the 200-hPa level.

the summer hemisphere and descent in the middle latitudes of both hemispheres. This result is shown in Figure 7 through the meridional streamfunction  $(\Psi)$  defined as

$$\Psi = \frac{2\pi a \cos(\phi)}{g} \int_{p}^{p_0} [\overline{v}] dp,$$

where  $[\bar{v}]$  is the time mean, zonal mean meridional wind, a is Earth's radius, g is gravity, p is pressure, and  $p_0$  is set as 1,000 hPa. As in nature, the summer hemisphere is associated with a weaker Hadley cell than in the winter hemisphere in all simulations (Figure 7). The Hadley cells expand in altitude with uniform warming. This result is illustrated with the  $-0.25 \times 10^{11}$  kg s<sup>-1</sup> and  $0.25 \times 10^{11}$  kg s<sup>-1</sup> contours (black lines in Figure 7). These contours are below 200 hPa in minus4K, around 200 hPa in CTL, and above 200 hPa in plus4K. Uppertropospheric divergence reach up to around 200 hPa in minus4K but nearly 100 hPa in plus4K, which is consistent with the upward expansion of the troposphere with uniform warming.

The Hadley cells also weaken with warming, although this is more pronounced in the winter hemisphere than in the summer hemisphere. This result is more readily seen in Figure 8, which shows the vertically integrated meridional streamfunction between 300 and 700 hPa following studies of the Hadley cell and the ITCZ (e.g., J. Lu et al., 2007; Byrne et al., 2018). The largest differences between experiments appear south of  $10^{\circ}$ N in association with the Southern Hemisphere Hadley cell. Peak mass transport decreases from 305 Gkg s<sup>-1</sup> in minus4K to 288 Gkg s<sup>-1</sup> in CTL and 266 in Gkg s<sup>-1</sup> in plus4K. The equivalent rates of change are non-linear across these three experiments because there is a -1.5% K<sup>-1</sup> change between minus4K to CTL and -1.9% K<sup>-1</sup> change between CTL and plus4K. Comprehensive climate model projections also show weakening Hadley cells in a future

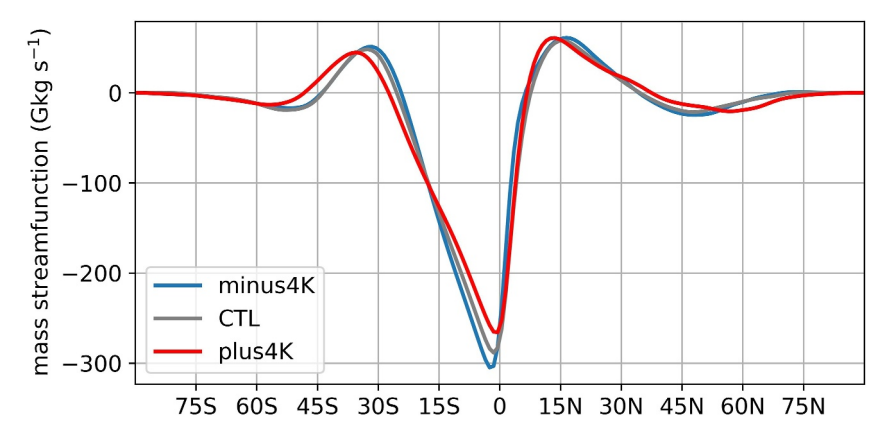


Figure 8. 300–700 hPa vertically-averaged meridional streamfunction from minus4K (blue), CTL (gray), and plus4K (red).

RIOS-BERRIOS ET AL. 12 of 25

warmer climate (J. Lu et al., 2007). Similarly, aquaplanet simulations with 4-K globally uniform warming show robust Hadley cell weakening and widening with warming (Medeiros et al., 2015).

Our simulations show a slight widening of the Hadley cells with globally uniform warming. The subtropical zero-streamfunction shifts from approximately  $24^{\circ}$ S in minus4K, to  $25^{\circ}$ S in CTL, and  $27^{\circ}$ S in plus4K (Figure 8). In the Northern Hemisphere, the zero crossing moves from  $34^{\circ}$ N in both minus4K and CTL to  $37^{\circ}$ N in plus4K (Figure 8). The equivalent rate of change is near or just below  $1^{\circ}$  K<sup>-1</sup>.

To further investigate the physical mechanisms behind the slight Hadley cell widening, we employed the theoretical scaling of Korty and Schneider (2008). Their scaling defines the subtropical terminus of the Hadley cell as the latitude where wave activity fluxes extend through the troposphere. This latitude can be identified by a supercriticality condition  $(S_c)$  given by

$$S_c = -\frac{f}{\beta} \frac{\partial_y \overline{\theta_s}}{\Delta_y},\tag{3}$$

where f is Coriolis,  $\beta$  is  $\frac{df}{df}$ ,  $\partial_y \overline{\theta_s}$  is the meridional gradient of time-mean, zonal-mean surface potential temperature, and  $\Delta_v$  is a bulk dry static stability. Even though this scaling was developed for dry atmospheres, it is a useful diagnostic that does not assume conservation of angular momentum. To determine  $S_c$ , we first identified the extratropical latitudes as the regions where eddy meridional heat fluxes exceeded 30% of its maximum, as done by Schneider and Walker (2006). We then found the latitude closest to the equator, in each hemisphere, where  $S_c$  first exceeded 0.63. This threshold is the same as in Korty and Schneider (2008), who found that value to be optimal for their set of idealized simulations. Our results are qualitatively independent of the precise threshold.

Results from this analysis confirm a widening Hadley cell with globally uniform ocean warming. The super-criticality is met at  $30.5^{\circ}$ S,  $31.5^{\circ}$ S,  $34.5^{\circ}$ S in minus4K, CTL, and plus4K, respectively. In the Northern Hemisphere, the supercriticality is met at  $36.5^{\circ}$ N,  $39.5^{\circ}$ N, and  $42.5^{\circ}$ N in minus4K, CTL, and plus4K, respectively. Although the estimated Hadley cell terminal latitudes are slightly different from the values estimated from the zero-crossing of the streamfunction, the scaling still captures a widening Hadley cell with warming. The resulting rates of changes are under  $1^{\circ}$  K $^{-1}$ .

Equation 3 predicts that changes in the Hadley cell width must arise from changes in the surface meridional temperature gradient or in the bulk dry static stability. Given that all simulations share the same meridional temperature gradient, the sole plausible mechanism is changes in the bulk dry static stability. Indeed, the static stability in the extratropics increases with warming (not shown, but it can be deduced from Figures 3a and 3b), thus explaining the slight Hadley cell widening in our experiments.

The ascending branch of the Hadley Cell, that is, the ITCZ, shows a non-linear strengthening with warming. This result was already noted in the previous subsection (Figure 5a). We quantitatively measured the ITCZ strength by two metrics: (a) the maximum time mean, zonal mean precipitation (from Figure 5a) and (b) a dynamics-based ITCZ strength metric following Byrne et al. (2018). The second metric is defined as

$$\omega_{ITCZ} = -g \frac{\Psi_{ITCZ}}{A_{ITCZ}},$$

where  $\Psi_{ITCZ}$  is the ITCZ mass transport and  $A_{ITCZ}$  is the ITCZ area defined as

$$A_{ITCZ} = 2\pi a^2 (\sin \phi_N - \sin \phi_s),$$

where  $\phi_n$  and  $\phi_s$  are the latitudes of the peak  $\Psi$  in each hemisphere. Both metrics capture the non-linear response of the ITCZ to warming (Figure 9a). As noted before, the maximum time mean, zonal mean rainfall rate increases by ~1% K<sup>-1</sup> from minus4K to CTL and by ~7% K<sup>-1</sup> from CTL to plus4K. Likewise, the dynamics-based metric shows a non-linear response, with a change of ~1.4% K<sup>-1</sup> from minus4K to CTL and ~3.2% K<sup>-1</sup> from CTL to plus4K.

RIOS-BERRIOS ET AL. 13 of 25

19422466, 2025, 10, Downloaded from https://agupubs.onlinelibrary.wiley.com/doi/10.1029/2025MS005119 by Kerry Emanuel , Wiley Online Library on [26/10/2025]

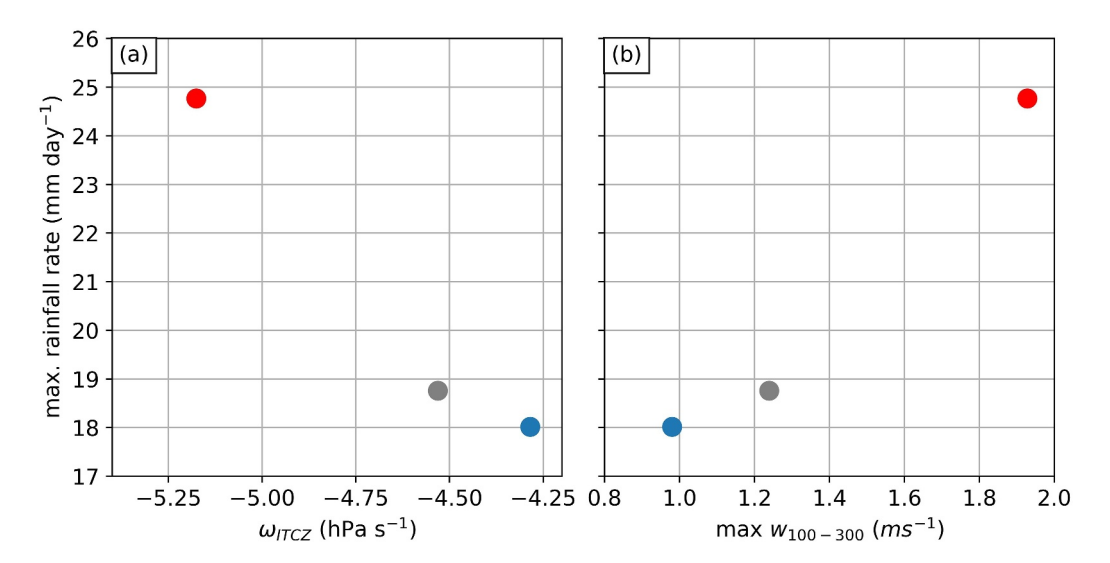


**Figure 9.** Comparison of maximum time mean, zonal mean rainfall rate versus (a) Intertropical Convergence Zone strength (see text for details) and (b) maximum time mean, zonal mean 100–300 hPa averaged vertical velocity. Blue, gray, and red colors represent minus4K, CTL, and plus4K, respectively.

The strong relationship between the two metrics of ITCZ strength suggest that changes in the time mean, zonal mean circulation are associated with changes in ascent and rainfall production. To further examine this, we evaluated the vertical velocity that is explicitly produced by the model equations as another metric of ITCZ strength (Figure 9b). We chose to average the vertical velocity between 100 and 300 hPa as this layer showed the largest difference between experiments. This metric also shows non-linear increases with warming, yielding a response of  $5.9\%~K^{-1}$  from minus4K to CTL and  $10.9\%~K^{-1}$  from CTL to plus4K. The Pearson's correlation coefficient between time mean, zonal mean peak rainfall and peak ascent is 0.99. Thus, while rainfall rates increase non-linearly with globally uniform warming, they increase linearly with upper-tropospheric vertical velocity.

To examine the physical processes between ITCZ strength (as measured by rainfall rate) and ocean warming, we followed P. Lu et al. (2018) to approximate the rainfall rate (p) by:

$$p = 0.0012\epsilon_p q_s w_+ \tag{4}$$

where 0.0012 is the ratio between dry-air density and liquid-water density,  $\epsilon_p$  is precipitation efficiency,  $q_s$  is saturated specific humidity,  $w_+$  is *upward* vertical velocity. Equation 4 implies that surface rainfall rate is proportional to the vertical flux of water vapor. This expression has been widely used for investigating rainfall during flash floods (Doswell et al., 1996), tropical cyclones (P. Lu et al., 2018), rainfall extremes (Wilson & Toumi, 2005), and in the ITCZ (Pendergrass, 2020). Equation 4 is typically evaluated at the height of a "moist layer" below 2 km above ground level or around 700 hPa. Here, we evaluated  $q_s$  and  $w_+$  using six-hourly output at approximately 1.5 km because MPAS-A uses geometric height as its vertical coordinate. Each variable is represented by its time mean, zonal mean value.

P. Lu et al. (2018) assumes a fixed  $\epsilon_p$  of 0.9 in tropical cyclones, which is not necessarily valid for all weather systems. We estimated  $\epsilon_p$  via the "large-scale precipitation efficiency 2" of Sui et al. (2007) given by

$$\epsilon_p = \frac{p}{\operatorname{sng}\left(\frac{\partial \overline{q_v}}{\partial t}\right) + \operatorname{sng}\left(\nabla \cdot \overline{q_v \overrightarrow{V}}\right) + \operatorname{sng}\left(\frac{\partial \overline{q_c}}{\partial t}\right) + \operatorname{sng}\left(\nabla \cdot \overline{q_c \overrightarrow{V}}\right) + E},$$

where p is precipitation rate as above,  $q_v$  is water vapor mixing ratio,  $q_c$  is total condensate mixing ratio, V is the three-dimensional wind vector, E is surface evaporation, and the overbars represent a vertical mass-weighted integral. This definition of  $\epsilon_p$  measures the rate of surface precipitation against the estimated production of

RIOS-BERRIOS ET AL. 14 of 25

19422466, 2025, 10, Downloaded from https://agupubs.onlinelibrary.wiley.com/doi/10.1029/2025MS005119 by Kerry Emanuel , Wiley Online Library on [26/10/2025]. See the Terms

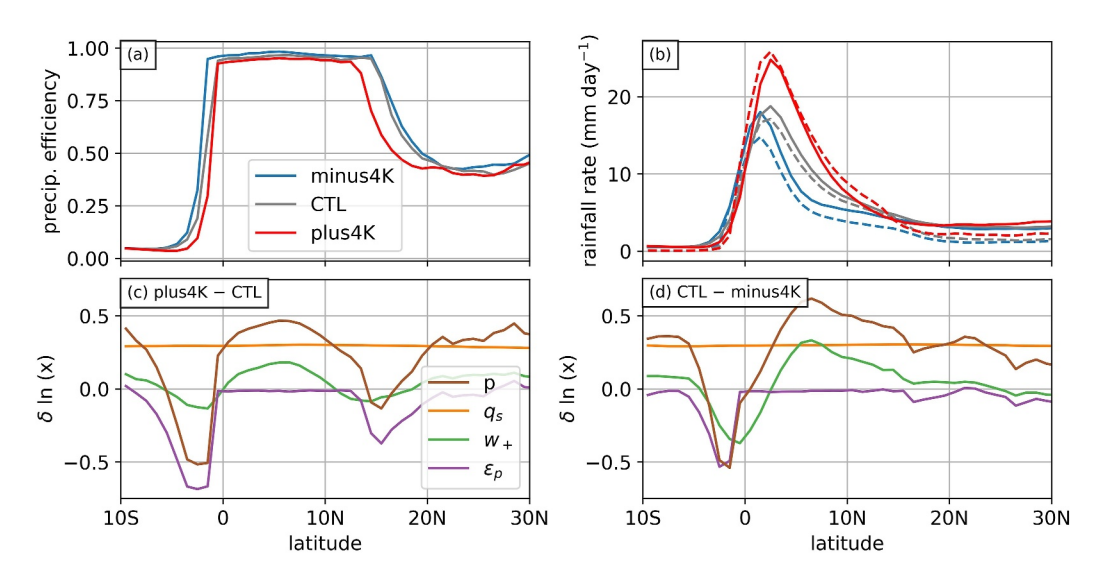


**Figure 10.** (a, b) Time mean, zonal mean (a) precipitation efficiency and (b) rainfall rates (solid) and approximated rainfall rate from Equation 4 (dashed). Blue, gray, and red colors represent minus4K, CTL, and plus4K, respectively. (c, d) The relative changes between (c) plus4K and CTL, and between (c) CTL and minus4K calculated from Equation 5. Brown lines represent approximated rainfall rate, orange lines represent specific humidity, green lines represent upward vertical velocity, and purple lines represent precipitation efficiency.

condensation via a combination of the water vapor and condensate budgets. Figure 10a shows the diagnosed  $\epsilon_p$ . All simulations show high efficiency in the tropics between 2.5°S–10°N, decaying toward low values outside the tropics. The atmosphere becomes less efficient with warming, but this issue will not be investigated further in this study.

Despite its simplicity, Equation 4 reasonably replicates the time-mean, zonal-mean rainfall rate in regions of high precipitation (Figure 10b). The approximation captures peak rainfall rates associated with the ITCZ and declining rainfall toward the subtropics. The approximation underestimates rainfall rates in minus4K and in CTL, but it overestimates rainfall rates in plus4K. This is likely due to the fixed height used in all simulations because the layer of converging water vapor increases with warming (not shown). Nonetheless, the approximation captures the general shape of the latitudinal rainfall rate profile in all simulations while also capturing increasing ITCZ rainfall with warming. Thus, Equation 4 is useful for explaining the ITCZ response to ocean warming in our simulations.

We expand this analysis by taking the natural logarithm and differentiating on each side of Equation 4 to obtain

$$\partial \ln p = \partial \ln \epsilon_p + \partial \ln w_+ + \partial \ln q_s, \tag{5}$$

which is equivalent to

$$\frac{\partial p}{p} = \frac{\partial \epsilon_p}{\epsilon_p} + \frac{\partial w_+}{w_+} + \frac{\partial q_s}{q_s}.$$

This expression relates the fractional changes in rainfall rate to the linear sum of fractional changes in precipitation efficiency, vertical velocity, and saturation specific humidity. Figures 10c and 10d show the changes of all terms of Equation 5. We show the difference between plus4K and CTL (Figure 10c) as well as the difference between CTL and minus4K (Figure 10d).

This analysis demonstrates that thermodynamic and dynamic processes exert distinct controls on the ITCZ strength response to warming. Rainfall rates decrease south of the ITCZ and increase within and north of the ITCZ with warming, consistent with the aforementioned discussion of Figure 5a. The *pattern* of rainfall changes follows closely after the pattern of  $w_+$  changes with decreasing ascent (or increasing descent) south of the ITCZ and increasing ascent within and north of the ITCZ. However, the *magnitude* of rainfall changes is likely also

RIOS-BERRIOS ET AL. 15 of 25

Table 2

Intertropical Convergence Zone Location as Defined by: (Left to Right) the Latitude of Zero Vertically-Averaged (300–700 hPa) Mass Streamfunction  $(\phi|_{\Psi=0})$ , the Latitude of Zero Mean Meridional Heat Transport (Also Known as the "Energy Flux Equator")  $(\phi|_{EFE})$ , the Latitude of Maximum Time Mean, Zonal Mean Rainfall Rate  $(\phi|_{pr=max})$ , and the Latitude of Maximum Time Mean, Zonal Mean 100–300 hPa Vertical Velocity  $(\phi|_{w=max})$ 

Experiment	$\phi _{\Psi=0}$	$\phiig _{EFE}$	$\phi \Big _{pr=\max}$	$\phi \Big _{w=\max}$
minus4K	6.3°N	2.7°N	1.5°N	1.5°N
CTL	7.6°N	3.6°N	2.5°N	2.5°N
plus4K	6.7°N	2.5°N	2.5°N	2.5°N

influenced by changes of  $q_s$ , which exhibits an increasing trend with nearly no latitudinal variability.  $\epsilon_p$  shows negligible changes within the ITCZ, validating previous assumptions of constant precipitation efficiency with warming (Muller et al., 2011). These results imply that the latitudinal structure of vertical velocity dictates the *pattern* of rainfall changes whereas both vertical velocity and saturated specific humidity influence the *magnitude* of those changes. Previous studies, although focused on rainfall extremes, agree that circulation changes (which include changes in vertical velocity) combined with water vapor changes largely influence the rainfall rates under different climates (Muller et al., 2011; O'Gorman, 2015; O'Gorman et al., 2021; O'Gorman & Schneider, 2009b).

Despite the robust signal in ITCZ strength, our simulations show an unclear response of ITCZ location with warming. We demonstrate this result using

four diagnostics: (a) the 300–700 hPa vertically averaged mass streamfunction, (b) the energy flux equator, (c) the time mean, zonal mean rainfall rate, and (c) the time mean, zonal mean vertical velocity vertically averaged between 100 and 300 hPa (Table 2). The first diagnostic defines the ITCZ location as the boundary between the northern and southern Hadley cells, which is given by a zero vertically averaged meridional streamfunction [Figure 1 of Byrne et al. (2018)]. Per this definition, the ITCZ is located at 6.3°N, 7.6°N, and 6.7°N in minus4K, CTL, and plus4K, respectively (Table 2). The second definition estimates the ITCZ location as the latitude where the mean meridional heat transport changes sign, indicating the export of energy away from the equator (Bischoff & Schneider, 2014; Schneider et al., 2014). We calculated the time mean, zonal mean meridional heat transport from instantaneous six-hourly fields as in Cox et al. (2024). The energy flux equator is located at 2.7°N, 3.6°N, and 2.5°N in minus4K, CTL, and plus4K, respectively (Table 2). However, defining the ITCZ as the location of maximum time mean, zonal mean rainfall rate yields locations of 1.5°N in minus4K, and 2.5°N in both CTL and plus4K (Table 2). Those values correspond exactly with the location of maximum 100–300-hPa time-mean, zonal-mean vertical velocity of each simulation (Table 2).

The simulated ITCZ response to warming is complex and sensitive to the metric used to define its position. While the ITCZ shifts poleward from minus4K to CTL in all metrics, its subsequent response in the plus4K simulation is inconsistent across different metrics. This metric-dependence aligns with previous work showing that the precipitation-based ITCZ is typically located equatorward of the energy flux equator (Adam et al., 2016; Donohoe et al., 2013). Discrepancies arise because circulation-based metrics (e.g., streamfunction) identify the broad region of ascent, while other metrics simply locate the peak in precipitation or vertical velocity.

We focus on the energy flux equator because a theoretical framework exists to explain its fluctuations (Adam et al., 2016; Bischoff & Schneider, 2014; Schneider et al., 2014). This framework predicts that the energy flux equator depends on the ratio between the mean meridional heat transport and the net energy input near the equator. Mathematically, this is given by

$$\delta_{ITCZ} = -\frac{1}{a} \frac{AHT_{EQ}}{I_{EQ}},\tag{6}$$

where  $AHT_{EQ}$  is the time mean, zonal mean meridional heat transport and  $I_{EQ}$  is the time mean, zonal mean energy forcing at the equator. This relationship explains the ITCZ location and its migrations across multiple timescales

 Table 3

 Summary of Intertropical Convergence Zone Energetics Analysis (See Text for Details)

Experiment	Cross-equatorial energy transport (PW)	Energy forcing at the equator $(W m^{-2})$	$\delta_{ITCZ}$
minus4K	-0.596	48.859	2.74°N
CTL	-0.729	52.352	3.13°N
plus4K	-0.592	52.931	2.51°N

*Note.* (Left to right) columns show the meridional energy transport at the equator, the total energy forcing at the equator, and the estimated ITCZ location from the energetics framework ( $\delta_{ITCZ}$ ).

RIOS-BERRIOS ET AL. 16 of 25

19422466, 2025, 10, Downloaded from https://agupubs.onlinelibrary.wiley.com/doi/10.1029/2025MS005119 by Kerry Enanuel, Wiley Online Library on [26/10/2025]. See the Term

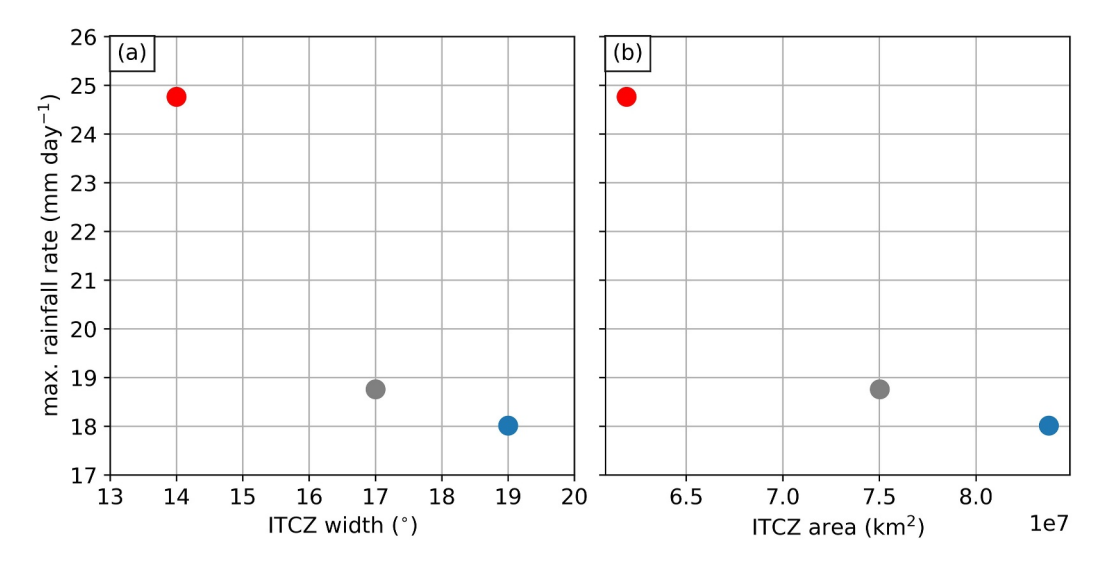


**Figure 11.** Comparison of maximum time mean, zonal mean rainfall rate versus (a) Intertropical Convergence Zone width and (b) area (see text for details). Blue, gray, and red colors represent minus4K, CTL, and plus4K, respectively.

(Adam et al., 2016; Schneider et al., 2014). We evaluated  $AHT_{EQ}$  and  $I_{EQ}$  as averages between 5°S to 5°N to account for uncertainty in the calculations. The results are listed in Table 3.

The theoretical framework accurately reproduces the non-linear trend in circulation-based ITCZ location. The estimated energy flux equator from Equation 6 is at  $2.74\,^{\circ}$ N,  $3.13\,^{\circ}$ N, and  $2.51\,^{\circ}$ N in minus4K, CTL, and plus4K. Evaluating the individual contributions from Equation 6 shows that  $AHT_{EQ}$  increases in magnitude by 5.5% K<sup>-1</sup> (-0.596 PW to -0.729 PW), whereas  $I_{EQ}$  increases by 1.8% K<sup>-1</sup> (48.859 W m<sup>-2</sup> to 52.352 W m<sup>-2</sup>) from minus4K to CTL. In contrast,  $AHT_{EQ}$  decreases in magnitude by 4.7% K<sup>-1</sup> from CTL to plus4K (-0.729 PW to -0.592 PW) and  $I_{EQ}$  is similar between these two experiments. Thus, the non-linear variations of the ITCZ location between our experiments stem primarily from non-linear changes in the mean meridional heat transport. This is likely due to the non-linear response of the mean climate to globally uniform warming in our simulations (Section 3.1) and is consistent with patterned changes in vertical velocity affecting patterned changes in ITCZ rainfall.

The diagnosis of time mean, zonal mean rainfall rates also suggest a narrowing ITCZ with warming. Rainfall rates decrease with warming at the northern and southern margins of the ITCZ (Figure 10). Following Byrne et al. (2018), we quantitatively defined the ITCZ width as

$$W_{ITCZ} = \phi_N - \phi_S,$$

where  $\phi_n$  and  $\phi_s$  are the latitudes of the peak  $\Psi$  in each hemisphere. We also used the definition of ITCZ area  $(A_{ITCZ})$  introduced earlier. These metrics capture the region of mean ascent and lower-tropospheric convergence, which extends over a wider area than relatively large precipitation rates (Byrne & Schneider, 2016).

Both of these metrics confirm a narrowing ITCZ and also exhibit a non-linear response to globally uniform warming (Figure 11). The ITCZ width decreases from  $19^{\circ}$  in minus4K to  $17^{\circ}$  in CTL and  $14^{\circ}$  in plus4K (Figure 11a), resulting in 2.7% K<sup>-1</sup> and 4.8% K<sup>-1</sup> changes, respectively. The ITCZ area shows nearly equivalent rates of changes. Both ITCZ width and area are strongly correlated with the ITCZ strength as measured by the maximum time mean, zonal mean precipitation rate (Pearson's correlation coefficient of 0.95). In other words, the ITCZ strengthens and narrows with warming in our simulations. This result is consistent with the "deep-tropics squeeze" noted in modeled climate projections (Lau & Kim, 2015), and with a larger number of models also integrated in the aquaplanet framework (Pendergrass et al., 2024). However, this result is inconsistent with the ITCZ weakening noted by most CMIP5 models (Byrne et al., 2018).

RIOS-BERRIOS ET AL. 17 of 25

19422466, 2025, 10, Downloaded from https://agupubs.onlinelibrary.wiley.com/doi/10.1029/2025MS00519 by Kerry Emanuel, Wiley Online Library on [26/10/2025]. See the Terms and Conditions (https://onlinelibrary.wiley.com/

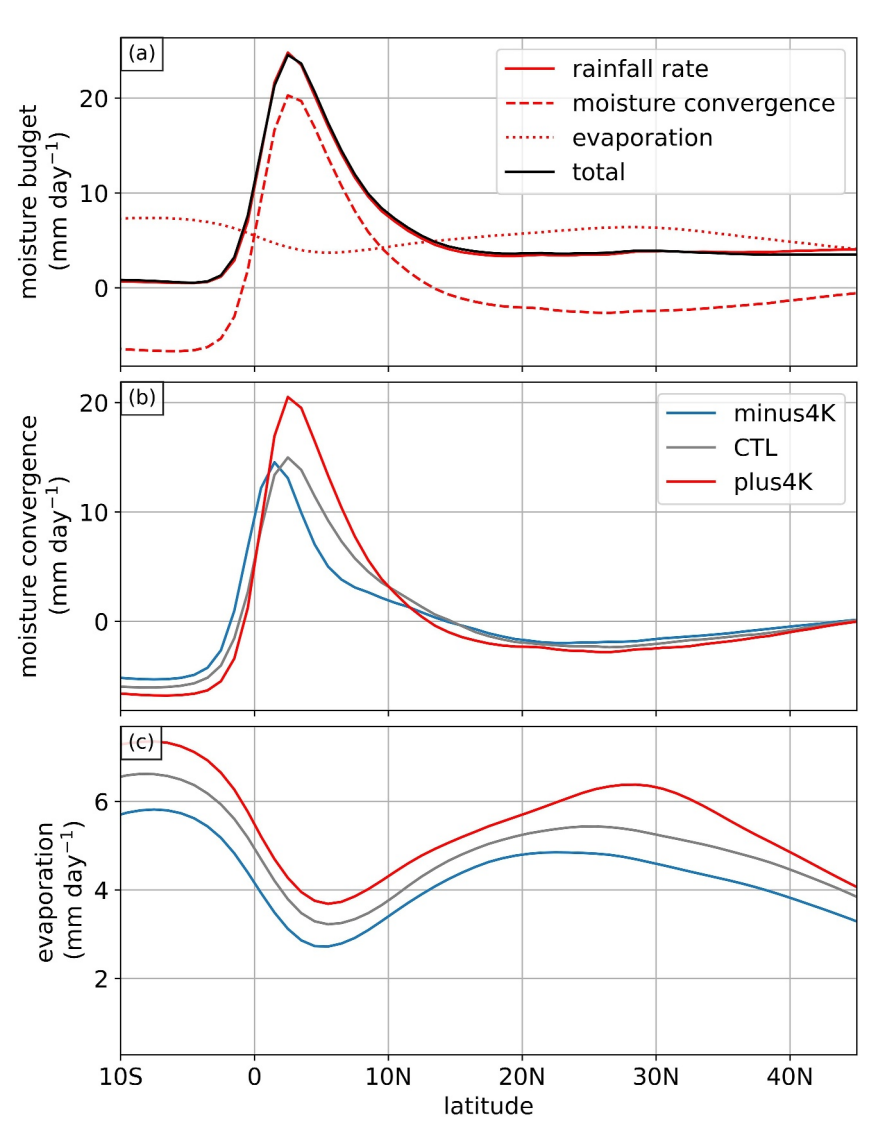


**Figure 12.** (a) Latitude profiles of time mean, zonal mean vertically integrated moisture budget from the plus4K simulation. Red lines show each budget term: rainfall rate (solid), moisture convergence (dashed), and evaporation (dotted). The black line shows the total sum of moisture convergence and evaporation. (b, c) Latitude profiles of (b) moisture convergence and (c) evaporation from (blue) minus4K, (black) CTL, and (red) plus4K.

The narrowing ITCZ with warming is associated with increased moisture divergence at the edges of the ITCZ. This result is demonstrated in Figure 12, which shows the total moisture budget. Assuming steady state, the time mean, zonal mean moisture budget can be expressed as

$$-\frac{\partial \langle \overline{vq_v} \rangle}{\partial y} = \langle p \rangle - \langle E \rangle, \tag{7}$$

where v is meridional wind,  $q_v$  is the water vapor mixing ratio, p is precipitation, E is evaporation, the brackets represent the time mean, zonal mean, and the overbar represents the mass-weighted vertical integral. Figure 12a demonstrates that Equation 7 is satisfied in our simulations as there is close agreement between the surface precipitation and the sum of evaporation and surface convergence. Examining the individual terms shows that moisture convergence increases within the ITCZ, while decreasing at the edges of the ITCZ with warming (Figure 12b). E increases at all latitudes (Figure 12c), but such increase is insufficient to counteract the dominant

RIOS-BERRIOS ET AL. 18 of 25

19422466, 2025, 10, Downloaded from https://agupubs.onlinelibrary.wiley.com/doi/10.1029/2025MS005119 by Kerry Emanuel , Wiley Online Library on [26/10/2025]. See the

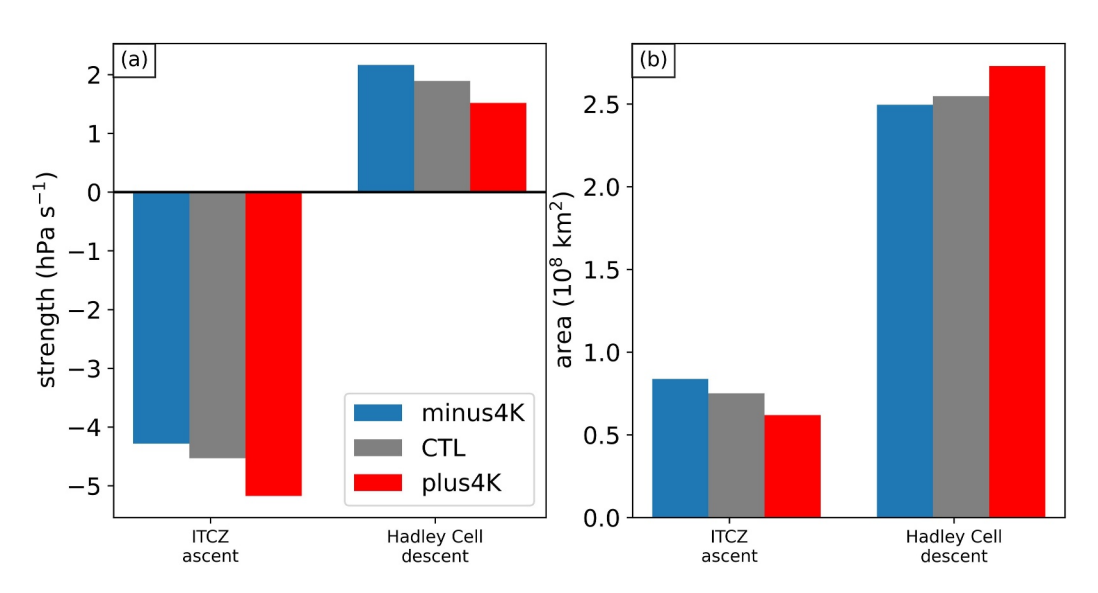


Figure 13. Diagnostics of (a) strength and (b) area of the Intertropical Convergence Zone ascent region and the Hadley cell descent region (see Equation 8) from (blue) minus 4K, (gray) CTL, and (red) plus 4K.

role of moisture convergence. Thus, the decreasing ITCZ size in our simulations likely results from expanding subsidence and drying in the subtropics (Figures 7a and 7b).

We considered alternative hypotheses, such as the energetic framework proposed by Byrne and Schneider (2016). Their framework suggests that ITCZ area changes, relative to Hadley cell subsidence area changes, are controlled by four processes: gross moist static stability, energy input, mean energy advection, and energy fluxes by transient eddies. We were unable to close the budget from Byrne and Schneider (2016), possibly indicating that the linear approximations made in the derivation are not satisfied in our simulations.

It may seem counterintuitive that the ITCZ strengthens and narrows, whereas the Hadley cell weakens and slightly expands with warming. However, this can be explained by mass conservation principles. The mass budget for the Hadley cell can be written following Byrne and Schneider (2016):

$$A_i \widetilde{\omega}_i = -A_d \widetilde{\omega}_d, \tag{8}$$

where A is area,  $\tilde{\omega}$  is strength as defined above, and the subscripts i and d stand for the ITCZ and the descending regions of the Hadley cell. Figure 13 shows these four quantities for each experiment. This figure illustrates that the ITCZ strengthens and narrows with warming in unison with an expanding and weakening descending region of the Hadley cell, which is expected from Equation 8. The ITCZ represents the small ascending region of the Hadley cell, but changes in the descending region are equally important.

#### 3.3. Tropical Rainfall Events

Using convection-permitting resolution within the tropics is beneficial to study the response of convective weather events to globally uniform warming. We focus generally on the response of tropical rainfall and tropical rainfall extremes, whereas future work should study the response of individual phenomena such as tropical cyclones and equatorial waves. To examine rainfall events, we constructed histograms of rainfall rates between 2.5°S–20°N (Figure 14). The distributions consider conservatively interpolated data to 1° and 0.25° and grid-scale (i.e., 3 km) data points to examine different spatial scales, which may respond differently to globally uniform warming (O'Gorman et al., 2021). We analyzed daily and six-hourly output to examine different timescales. Additionally, on each spatial and temporal scale, we calculated the fraction of data points with 0 rainfall rates by dividing the number of such points by the total number of points on that scale. Results are based on millions or even billions of samples (see counts in Figure 14).

A globally uniform warming affects the distribution of tropical rainfall in a manner consistent with the effects on the tropical climate (Figure 14). The fractions of very high and very low rainfall rates increase with warming,

RIOS-BERRIOS ET AL. 19 of 25

19422466, 2025, 10, Downloaded from https://agupubs.onlinelibrary.wiley.com/doi/10.1029/2025MS005119 by Kerry Emanuel , Wiley Online Library on [26/10/2025]. See the Term

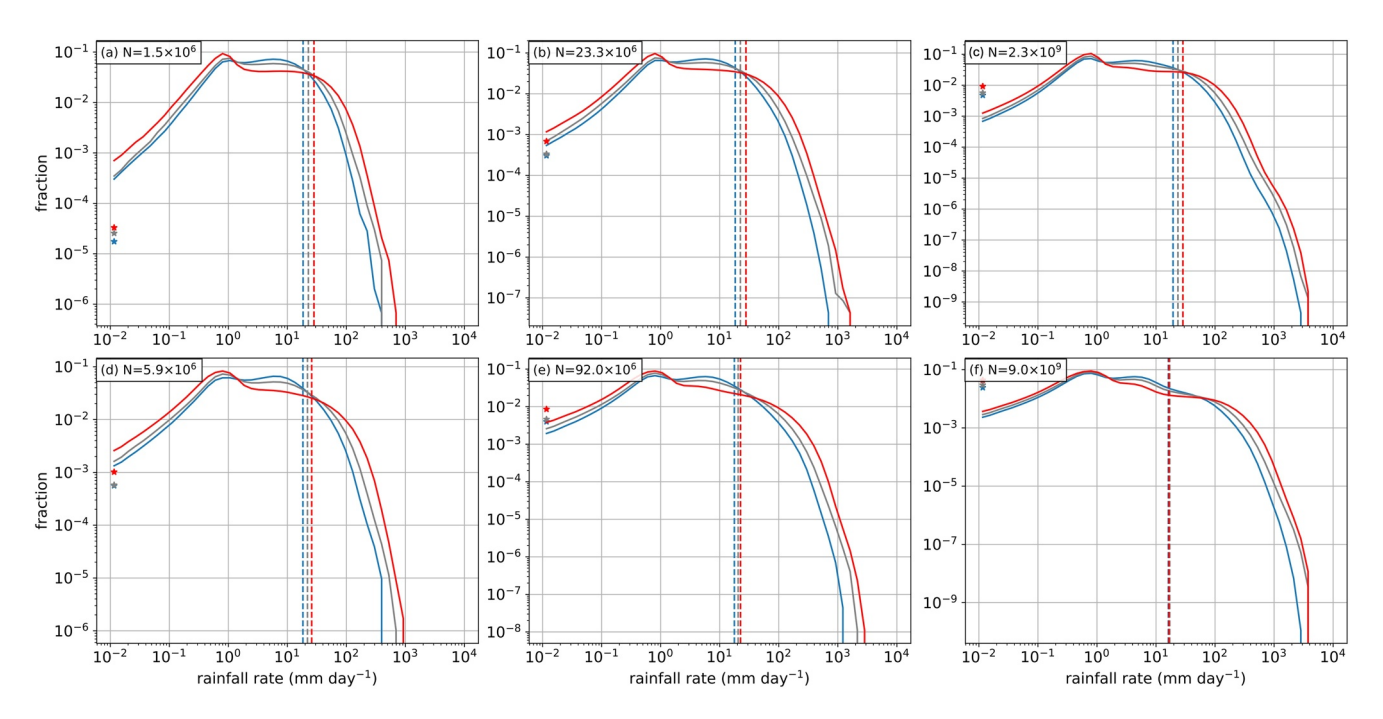


Figure 14. Normalized histograms of (a–c) daily and (d–f) 6-hourly rainfall rates between  $2.5^{\circ}S-20^{\circ}N$  from the (blue) minus4K, (gray) CTL, and (red) plus4K experiments. Panels (a), (b), (d), and (e) show histograms from conservatively interpolated output on a  $1^{\circ} \times 1^{\circ}$  and  $0.25^{\circ} \times 0.25^{\circ}$  latitude-longitude grid. Panels (c) and (f) show histograms from the native (i.e., 3 km) model output. Stars show the fraction on non-rainy grid points, dashed lines mark the 90th percentile of each histogram, and the sample size of each panel is next to the panel label.

while the fractions of intermediate precipitation rates decrease with warming. The crossover between decreasing to increasing fraction of rainfall rates occurs at approximately the 90th percentile (dashed lines in Figure 14), which is indicative of stronger precipitation extremes with warming. The fraction of non-rainy points also

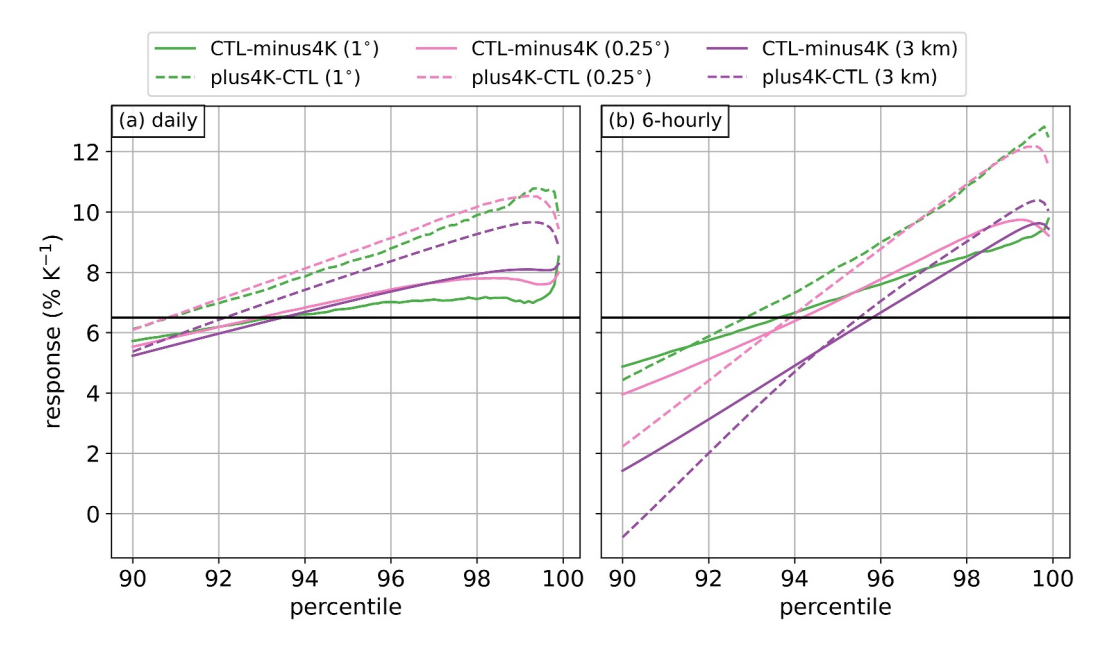


Figure 15. Changes in the top tenth percentiles of non-zero (a) daily and (b) six-hourly rainfall rates between CTL and minus 4K (solid) and between plus 4K and CTL (dashed). Colors represent different horizontal resolution of the model output: green depicts  $1^{\circ}$ , pink depicts  $0.25^{\circ}$ , and purple represents the native 3-km output. The black line shows the approximate Clausius-Clapeyron scaling.

RIOS-BERRIOS ET AL. 20 of 25

increases with warming, especially between CTL and plus4K (stars in Figure 14). Thus, rainy regions experience heavier rainfall rates whereas dry regions get drier with warming.

Changes in the distribution of tropical rainfall are consistent across all temporal and spatial scales considered, but the precise magnitude of the changes between experiments depends on the spatiotemporal scales. Figure 15 quantifies the percent change of the top percentiles between minus4K and CTL and between CTL and plus4K. We focus on the high percentiles, which represent the extremes. On daily timescales, nearly all extremes at or above the 91–93rd percentile increase at a rate exceeding Clausius-Clapeyron scaling (i.e., at or above 6.5% K<sup>-1</sup>) (Figure 15a). Consistent with the non-linear response discussed earlier, daily tropical precipitation extremes also increase non-linearly with warming because the rates of changes are larger between CTL and plus4K than between minus4K and CTL. Results from the six-hourly extremes are more complex than their daily counterparts. The coarse grained data exhibits larger rates of change than the 3-km output at nearly all percentiles (Figure 15b). The 90th percentile shows an increase of 2%–5% K<sup>-1</sup> in the 1° and 0.25° output, while the 3-km native output remains almost unchanged. Super Clausius-Clapeyron rates of change appear only above the 95th percentile when considering the 3-km model output, whereas they appear at lower percentiles in the coarse grained data. These results are consistent with a previous study (O'Gorman et al., 2021), and they warn about considerations of different spatiotemporal scales when analyzing tropical precipitation extremes.

## 4. Summary and Discussion

This study examined the response of tropical climate and extreme precipitation to globally uniform SST warming in aquaplanet simulations with convection-permitting resolution in the tropics. The simulations bridge a gap between climate and weather models by using a global framework while also resolving the convective-scale dynamics of tropical weather systems (Figure 1). Three simulations were performed with SSTs mimicking current boreal summer conditions (CTL) and SSTs either decreased (minus4K) or increased (plus4K) uniformly by 4 K at all grid points. This experimental setup allows for an analysis of the response of both climate and weather to ocean temperature. Moreover, using boreal summer conditions allows for more Earth-like Hadley cells and promotes tropical cyclones, which differentiates this configuration from most aquaplanet experiments. Here, we focused primarily on the global climate, tropical climate, and tropical rainfall events.

Results showed that the tropical climate responds in various ways to the ocean temperature. The tropical troposphere warms and expands with warming, thus lifting the melting level and the tropopause. The Hadley cell weakens and slightly expands, whereas the ITCZ strengthens and narrows with globally uniform warming. This ITCZ strengthening rate was replicated by an approximation given by the upward flux of water vapor, which further showed that patterned changes in the vertical velocity are largely responsible for the pattern of changes of rainfall rates. Changes in specific humidity primarily contribute to magnitude changes time-mean, zonal-mean rainfall rate changes. Changes in ITCZ location are sensitive to the metric used to define its position—all metrics show a poleward migration from minus4K to CTL, but the response from CTL to plus4K varies with different definitions of ITCZ position. Nonetheless, the ITCZ narrows with warming, consistent with drier and more expansive subtropics. The upper-tropospheric jets move equatorward and strengthen with warming, likely due to the warming tropical troposphere in combination with a cooling polar stratosphere in our configuration with globally uniform warming. Clouds, especially icy clouds, respond non-linearly to warming. This non-linear response likely affects the TOA radiative flux budget, which also shows non-linear changes with warming.

Extreme tropical precipitation also responds in various ways to the changing ocean temperature. Rainfall extremes exceeding the 90th percentile *increase* in magnitude, the fraction of very low rainfall rates and non-rainy points also *increase*, and the fraction of intermediate rainfall rates *decrease* with ocean warming. Tropical precipitation extremes at or above the 92nd or 95th percentiles (depending on the temporal and spatial resolution) increase at a rate exceeding Clausius-Clapeyron scaling, which motivates further research into understanding the physical processes enabling those extremes.

Further investigation is needed to get a holistic understanding of how dynamic, thermodynamic, and microphysics processes change rainfall production with globally uniform warming. Such investigation should also account for the properties of weather systems—tropical cyclones, mesoscale convective systems, etc.—that produce the rainfall extremes. Those systems could manifest as a more organized convective state. Since the role of convective organization on modulating precipitation extremes is unclear (Pendergrass et al., 2024), it is crucial to

RIOS-BERRIOS ET AL. 21 of 25

examine how ocean warming influences tropical weather systems and their organization. This will elucidate the complex relationship between convective organization, precipitation extremes, and the changing climate.

A common theme throughout this study was a non-linear response of various factors to ocean warming. The Hadley cell maximum transport decreased by  $7.9\%~K^{-1}$  between minus4K to CTL but by  $5.7\%~K^{-1}$  between CTL and plus4K. In contrast, the ITCZ strength, measured by the maximum time mean, zonal mean rainfall rate, increased by  $\sim 1\%~K^{-1}$  from minus4K to CTL but by  $\sim 7\%^{-1}$  from CTL to plus4K. Other ITCZ characteristics, including its cloud water path and maximum upper-tropospheric vertical velocity, also increased more strongly from CTL to plus4K than from minus4K to CTL. Likewise, the magnitude of rainfall extremes increased more strongly between CTL to plus4K than between minus4K and CTL, especially at daily timescales. This might be because the transformation from a constant change in SST to the change in sea surface saturation entropy is non-linear. The non-linear changes underscore the importance of having more than two comparable scenarios when assessing the quantitative response of atmospheric phenomena to climate change. Past changes (e.g., from paleoclimate evidence) may not properly constrain future changes, and similarly estimates of current trends should not be extrapolated to future warming without accounting for the non-linearities.

Although these experiments are insightful, our results are limited by our idealized modeling approach and the relatively short integration time. The absence of land, sea-ice, seasons, and radiatively active aerosols removes important interactions within the Earth system. The simulations neither produce the Madden-Julian Oscillation nor contain—by design—El Niño or La Niña events. At the same time, the simulations use a simple ocean mixed layer depth model that is far simpler than the three-dimensional, dynamic oceans in nature. Our approach to investigating the response to warming only considers globally uniform cooling and warming, but patterned changes that vary with both latitude and longitude are likely important in determining local weather variability due to climate change. We also kept the CO<sub>2</sub> concentration fixed and did not account for the impact of increasing CO<sub>2</sub> on the thermodynamic structure of the atmosphere. Lastly, our analysis was limited to only 6 months and a single combination of physics packages due to the expensive computational cost and large storage needs of our simulations. Future work should consider the sensitivity of our results to the choice of physics packages.

Despite the aforementioned limitations, these simulations are useful for exploring the sensitivity of tropical climate and weather systems to uniform ocean warming. Our global configuration captures the global climate system, while the variable-resolution mesh with convection-permitting resolution in the tropics captures the critical convective-scale dynamics of tropical weather systems (Figure 1). This study has set the stage for future studies by documenting the response of the global climate, tropical climate, and extreme precipitation to globally uniform warming. Other studies should consider using these simulations to study the properties of tropical cyclones, tropical waves, and other tropical weather systems as well as their response to ocean warming.

# **Conflict of Interest**

The authors declare no conflicts of interest relevant to this study.

# **Data Availability Statement**

The interpolated model output is readily accessible from Rios-Berrios (2025a). The native model output, due to its massive size of approximately 300 TB, cannot be hosted in the same manner and is therefore only distributed upon request. All code used for data analysis in this manuscript is publicly available from Rios-Berrios (2025b).

#### References

Adam, O., Bischoff, T., & Schneider, T. (2016). Seasonal and interannual variations of the energy flux equator and ITCZ. Part I: Zonally averaged ITCZ position. *Journal of Climate*, 29(9), 3219–3230. https://doi.org/10.1175/jcli-d-15-0512.1

Asadieh, B., & Krakauer, N. Y. (2015). Global trends in extreme precipitation: Climate models versus observations. *Hydrology and Earth System Sciences*, 19(2), 877–891. https://doi.org/10.5194/hess-19-877-2015

Ballinger, A. P., Merlis, T. M., Held, I. M., & Zhao, M. (2015). The sensitivity of tropical cyclone activity to off-equatorial thermal forcing in aquaplanet simulations. *Journal of the Atmospheric Sciences*, 72(6), 2286–2302. https://doi.org/10.1175/JAS-D-14-0284.1

Bao, J., Stevens, B., Kluft, L., & Muller, C. (2024). Intensification of daily tropical precipitation extremes from more organized convection. Science Advances, 10(8), eadj6801. https://doi.org/10.1126/sciadv.adj6801

Bartana, H., Garfinkel, C. I., Shamir, O., & Rao, J. (2022). Projected future changes in equatorial wave spectrum in CMIP6. Climate Dynamics, 60(11–12), 3277–3289. https://doi.org/10.1007/s00382-022-06510-y

Birner, T., Davis, S. M., & Seidel, D. J. (2014). The changing width of Earth's tropical belt. *Physics Today*, 67(12), 38–44. https://doi.org/10.1063/pt.3.2620

# Acknowledgments

We are grateful to Drs. Erin Dougherty, Jonathan Martinez, Kelly M. Núñez Ocasio, and Andreas Prein for their helpful input to this study. Comments from the Editor, Dr. Tapio Schneider, and an anonymous reviewer helped improve this manuscript. This work was possible thanks to an Accelerated Scientific Discovery supercomputing allocation provided by NSF NCAR's Computational Information Systems Laboratory. This material is based upon work supported by the NSF National Center for Atmospheric Research, which is a major facility sponsored by the U.S. National Science Foundation under Cooperative Agreement No. 1852977. BM also acknowledges support by the U.S. Department of Energy, Office of Science, Office of Biological & Environmental Research, Regional and Global Model Analysis component of the Earth and Environmental System Modeling Program under Award Number DE-SC0022070 and NSF IA 1947282

RIOS-BERRIOS ET AL. 22 of 25



# **Journal of Advances in Modeling Earth Systems**

- 10.1029/2025MS005119
- Bischoff, T., & Schneider, T. (2014). Energetic constraints on the position of the Intertropical Convergence Zone. *Journal of Climate*, 27(13), 4937–4951. https://doi.org/10.1175/icli-d-13-00650.1
- Bony, S., & Dufresne, J. (2005). Marine boundary layer clouds at the heart of tropical cloud feedback uncertainties in climate models. *Geophysical Research Letters*, 32(20), L20806. https://doi.org/10.1029/2005g1023851
- Bryan, G. H., & Morrison, H. (2012). Sensitivity of a simulated squall line to horizontal resolution and parameterization of microphysics. *Monthly Weather Review*, 140(1), 202–225. https://doi.org/10.1175/MWR-D-11-00046.1
- Byrne, M. P., Pendergrass, A. G., Rapp, A. D., & Wodzicki, K. R. (2018). Response of the Intertropical Convergence Zone to Climate change: Location, width, and strength. *Current Climate Change Reports*, 4(4), 355–370. https://doi.org/10.1007/s40641-018-0110-5
- Byrne, M. P., & Schneider, T. (2016). Narrowing of the ITCZ in a warming climate: Physical mechanisms. *Geophysical Research Letters*, 43(21), 11350. https://doi.org/10.1002/2016g1070396
- Cess, R. D., Potter, G. L., Blanchet, J. P., Boer, G. J., Del Genio, A. D., Déqué, M., et al. (1990). Intercomparison and interpretation of climate feedback processes in 19 atmospheric general circulation models. *Journal of Geophysical Research*, 95(D10), 16601–16615. https://doi.org/10.1029/id095id10p16601
- Chemke, R., & Yuval, J. (2023). Human-induced weakening of the Northern Hemisphere tropical circulation. *Nature*, 617(7961), 529–532. https://doi.org/10.1038/s41586-023-05903-1
- Computational and Information Systems Laboratory. (2023). Derecho: HPE cray EX cluster. UCAR/NCAR. https://doi.org/10.5065/QX9A-PG09
- Cox, T., Donohoe, A., Armour, K. C., Roe, G. H., & Frierson, D. M. W. (2024). A new method for calculating instantaneous atmospheric heat transport. *Journal of Climate*, 37(17), 4337–4346. https://doi.org/10.1175/jcli-d-23-0521.1
- Curcic, M., & Haus, B. K. (2020). Revised estimates of ocean surface drag in strong winds. Geophysical Research Letters, 47(10), e2020GL087647. https://doi.org/10.1029/2020gl087647
- Donohoe, A., Marshall, J., Ferreira, D., & Mcgee, D. (2013). The relationship between ITCZ location and cross-equatorial atmospheric heat transport: From the seasonal cycle to the last glacial maximum. *Journal of Climate*, 26(11), 3597–3618. https://doi.org/10.1175/jcli-d-12-004671
- Doswell, C. A., Brooks, H. E., & Maddox, R. A. (1996). Flash flood forecasting: An ingredients-based methodology. Weather and Forecasting, 11(4), 560–581. https://doi.org/10.1175/1520-0434(1996)011/0560:fffaib)2.0.co;2
- Dufresne, J.-L., & Bony, S. (2008). An assessment of the primary sources of spread of global warming estimates from coupled atmosphere–ocean models. *Journal of Climate*, 21(19), 5135–5144. https://doi.org/10.1175/2008jcli2239.1
- Emanuel, K. A., David Neelin, J., & Bretherton, C. S. (1994). On large-scale circulations in convecting atmospheres. *The Quarterly Journal of the Royal Meteorological Society*, 120(519), 1111–1143. https://doi.org/10.1002/qj.49712051902
- Feng, Z., Leung, L. R., Liu, N., Wang, J., Houze, R. A., Li, J., et al. (2021). A global high-resolution mesoscale convective system database using satellite-derived cloud tops, surface precipitation, and tracking. *Journal of Geophysical Research: Atmospheres*, 126(8), e2020JD034202. https://doi.org/10.1029/2020jd034202
- Held, I. M., & Soden, B. J. (2006). Robust responses of the hydrological cycle to global warming. *Journal of Climate*, 19(21), 5686–5699. https://doi.org/10.1175/jcli3990.1
- Hong, S.-Y., Dudhia, J., & Chen, S.-H. (2004). A revised approach to ice microphysical processes for the bulk parameterization of clouds and precipitation. *Monthly Weather Review*, 132(1), 103–120. https://doi.org/10.1175/1520-0493(2004)132(0103:ARATIM)2.0.CO;2
- Hu, Y., & Fu, Q. (2007). Observed poleward expansion of the Hadley circulation since 1979. Atmospheric Chemistry and Physics, 7(19), 5229–5236. https://doi.org/10.5194/acp-7-5229-2007
- Huang, B., Liu, C., Banzon, V., Freeman, E., Graham, G., Hankins, B., et al. (2021). Improvements of the Daily Optimum Interpolation Sea Surface Temperature (DOISST) version 2.1. *Journal of Climate*, 34(8), 2923–2939. https://doi.org/10.1175/jcli-d-20-0166.1
- Iacono, M. J., Delamere, J. S., Mlawer, E. J., Shephard, M. W., Clough, S. A., & Collins, W. D. (2008). Radiative forcing by long-lived greenhouse gases: Calculations with the AER radiative transfer models. *Journal of Geophysical Research*, 113(D13), D13103. https://doi.org/10.1029/ 2008JD009944
- Igel, A. L., Igel, M. R., & van den Heever, S. C. (2015). Make it a double? Sobering results from simulations using single-moment microphysics schemes. *Journal of the Atmospheric Sciences*, 72(2), 910–925. https://doi.org/10.1175/JAS-D-14-0107.1
- Judt, F., & Rios-Berrios, R. (2021). Resolved convection improves the representation of equatorial waves and tropical rainfall variability in a global nonhydrostatic model. Geophysical Research Letters, 48(14), e2021GL093265, https://doi.org/10.1029/2021GL093265
- Klemp, J. B., Dudhia, J., & Hassiotis, A. D. (2008). An upper gravity-wave absorbing layer for NWP applications. *Monthly Weather Review*, 136(10), 3987–4004. https://doi.org/10.1175/2008mwr2596.1
- Knutson, T., Camargo, S. J., Chan, J. C. L., Emanuel, K., Ho, C.-H., Kossin, J., et al. (2020). Tropical cyclones and climate change assessment: Part II: Projected response to anthropogenic warming. *Bulletin America Meteorology Social*, 101(3), E303–E322. https://doi.org/10.1175/bams-d-18-0194.1
- Korty, R. L., & Schneider, T. (2008). Extent of Hadley circulations in dry atmospheres. Geophysical Research Letters, 35(23), L23803. https://doi.org/10.1029/2008gl035847
- Lau, W. K. M., & Kim, K.-M. (2015). Robust Hadley circulation changes and increasing global dryness due to CO<sub>2</sub> warming from CMIP5 model projections. *Proceedings of the National Academy of Sciences*, 112(12), 3630–3635. https://doi.org/10.1073/pnas.1418682112
- Levitus, S. (1982). Climatological atlas of the world ocean (p. 90). U.S. Government Printing Office.
- Lionello, P., D'Agostino, R., Ferreira, D., Nguyen, H., & Singh, M. S. (2024). The Hadley circulation in a changing climate. *Annals of the New York Academy of Sciences*, 1534(1), 69–93. https://doi.org/10.1111/nyas.15114
- Loeb, N. G., Doelling, D. R., Wang, H., Su, W., Nguyen, C., Corbett, J. G., et al. (2018). Clouds and the Earth's radiant energy system (CERES) energy balanced and filled (EBAF) top-of-atmosphere (TOA) edition-4.0 data product. *Journal of Climate*, 31(2), 895–918. https://doi.org/10.1175/jcli-d-17-0208.1
- Lu, J., Vecchi, G. A., & Reichler, T. (2007). Expansion of the Hadley cell under global warming. Geophysical Research Letters, 34(6), L06805. https://doi.org/10.1029/2006g1028443
- Lu, P., Lin, N., Emanuel, K., Chavas, D., & Smith, J. (2018). Assessing hurricane rainfall mechanisms using a physics-based model: Hurricanes Isabel (2003) and Irene (2011). *Journal of the Atmospheric Sciences*, 75(7), 2337–2358. https://doi.org/10.1175/jas-d-17-0264.1
- Lucas, C., Timbal, B., & Nguyen, H. (2013). The expanding tropics: A critical assessment of the observational and modeling studies. WIREs Climate Change, 5(1), 89–112. https://doi.org/10.1002/wcc.251
- Medeiros, B., Stevens, B., & Bony, S. (2015). Using aquaplanets to understand the robust responses of comprehensive climate models to forcing. Climate Dynamics, 44(7–8), 1957–1977. https://doi.org/10.1007/s00382-014-2138-0

RIOS-BERRIOS ET AL. 23 of 25



# **Journal of Advances in Modeling Earth Systems**

- 10.1029/2025MS005119
- Medeiros, B., Stevens, B., Held, I. M., Zhao, M., Williamson, D. L., Olson, J. G., & Bretherton, C. S. (2008). Aquaplanets, climate sensitivity, and low clouds. *Journal of Climate*, 21(19), 4974–4991. https://doi.org/10.1175/2008jcti1995.1
- Merlis, T. M., Cheng, K.-Y., Guendelman, I., Harris, L., Bretherton, C. S., Bolot, M., et al. (2024). Climate sensitivity and relative humidity changes in global storm-resolving model simulations of climate change. *Science Advances*, 10(26), eadn5217. https://doi.org/10.1126/sciadv.adn5217
- Mitas, C. M., & Clement, A. (2006). Recent behavior of the Hadley cell and tropical thermodynamics in climate models and reanalyses. Geophysical Research Letters, 33(1), L01810. https://doi.org/10.1029/2005g1024406
- Mlawer, E. J., Taubman, S. J., Brown, P. D., Iacono, M. J., & Clough, S. A. (1997). Radiative transfer for inhomogeneous atmospheres: RRTM, a validated correlated-k model for the longwave. *Journal of Geophysical Research*, 102(D14), 16663–16682. https://doi.org/10.1029/97jd00237
- Moncrieff, M. W. (2019). Toward a dynamical foundation for organized convection parameterization in GCMs. *Geophysical Research Letters*, 46(23), 14103–14108. https://doi.org/10.1029/2019gl085316
- Moncrieff, M. W., & Liu, C. (2006). Representing convective organization in prediction models by a hybrid strategy. *Journal of the Atmospheric Sciences*, 63(12), 3404–3420. https://doi.org/10.1175/jas3812.1
- Morrison, H., Thompson, G., & Tatarskii, V. (2009). Impact of cloud microphysics on the development of trailing stratiform precipitation in a simulated squall line: Comparison of one- and two-moment schemes. *Monthly Weather Review*, 137(3), 991–1007. https://doi.org/10.1175/2008mwr2556.1
- Muller, C. J., & O'Gorman, P. A. (2011). An energetic perspective on the regional response of precipitation to climate change. *Nature Climate Change*, 1(5), 266–271. https://doi.org/10.1038/nclimate1169
- Muller, C. J., O'Gorman, P. A., & Back, L. E. (2011). Intensification of precipitation extremes with warming in a cloud-resolving model. *Journal of Climate*, 24(11), 2784–2800. https://doi.org/10.1175/2011jcli3876.1
- Nesbitt, S. W., Cifelli, R., & Rutledge, S. A. (2006). Storm morphology and rainfall characteristics of TRMM precipitation features. *Monthly Weather Review*, 134(10), 2702–2721. https://doi.org/10.1175/mwr3200.1
- O'Gorman, P. A. (2012). Sensitivity of tropical precipitation extremes to climate change. *Nature Geoscience*, 5(10), 697–700. https://doi.org/10.1038/ngeo1568
- O'Gorman, P. A. (2015). Precipitation extremes under climate change. *Current Climate Change Reports*, *I*(2), 49–59. https://doi.org/10.1007/
- s40641-015-0009-3

  O'Gorman, P. A., Li, Z., Boos, W. R., & Yuval, J. (2021). Response of extreme precipitation to uniform surface warming in quasi-global aquaplanet simulations at high resolution. *Philosophical Transactions of the Royal Society A*, 379(2195), 20190543. https://doi.org/10.1098/rsta.2019.0543
- O'Gorman, P. A., & Schneider, T. (2009a). The physical basis for increases in precipitation extremes in simulations of 21st-century climate change. *Proceedings of the National Academy of Sciences*, 106(35), 14773–14777. https://doi.org/10.1073/pnas.0907610106
- O'Gorman, P. A., & Schneider, T. (2009b). Scaling of precipitation extremes over a wide range of climates simulated with an idealized GCM. Journal of Climate, 22(21), 5676–5685. https://doi.org/10.1175/2009jcli2701.1
- Pendergrass, A. G. (2020). Changing degree of convective organization as a mechanism for dynamic changes in extreme precipitation. *Current Climate Change Reports*, 6(2), 47–54. https://doi.org/10.1007/s40641-020-00157-9
- Pendergrass, A. G., Byrne, M. P., Watt-Meyer, O., Maher, P., & Webb, M. J. (2024). Impact of ITCZ width on global climate: ITCZ-MIP. Geoscientific Model Development, 17(16), 6365–6378. https://doi.org/10.5194/gmd-17-6365-2024
- Pollard, R. T., Rhines, P. B., & Thompson, R. O. R. Y. (1973). The deepening of the wind-mixed layer. Geophysical Fluid Dynamics, 4(4), 381–404. https://doi.org/10.1080/03091927208236105
- Prein, A. F., & Heymsfield, A. J. (2020). Increased melting level height impacts surface precipitation phase and intensity. *Nature Climate Change*, 10(8), 771–776. https://doi.org/10.1038/s41558-020-0825-x
- Rackow, T., Pedruzo-Bagazgoitia, X., Becker, T., Milinski, S., Sandu, I., Aguridan, R., et al. (2025). Multi-year simulations at kilometre scale with the Integrated Forecasting System coupled to FESOM2.5 and NEMOv3.4. Geoscientific Model Development, 18(1), 33–69. https://doi.org/10.5194/gmd-18-33-2025
- Rios-Berrios, R. (2025a). MPAS-A aquaplanet simulations with different sea-surface temperatures. UCAR/NCAR Research Data Archive. https://doi.org/10.5065/9NCV-EC03
- Rios-Berrios, R. (2025b). rosimarwxASD\_gencirc: Initial release (v1.0) [Software]. Zenodo. https://doi.org/10.5281/ZENODO.15028519
- Rios-Berrios, R., Bryan, G. H., Medeiros, B., Judt, F., & Wang, W. (2022). Differences in tropical rainfall in aquaplanet simulations with resolved or parameterized deep convection. *Journal of Advances in Modeling Earth Systems*, 14(5), e2021MS002902. https://doi.org/10.1029/ 2021MS002902
- Rios-Berrios, R., Davis, C. A., & Martinez, J. (2023). Tropical cyclones and equatorial waves in a convection-permitting aquaplanet simulation with off-equatorial SST maximum. *Journal of Advances in Modeling Earth Systems*, 15(10), e2023MS003723. https://doi.org/10.1029/2023ms003723
- Rios-Berrios, R., Judt, F., Bryan, G., Medeiros, B., & Wang, W. (2023). Three-dimensional structure of convectively coupled equatorial waves in aquaplanet experiments with resolved or parameterized convection. *Journal of Climate*, 36(9), 2895–2915. https://doi.org/10.1175/jcli-d-22-0422.1
- Rios-Berrios, R., Medeiros, B., & Bryan, G. H. (2020). Mean climate and tropical rainfall variability in aquaplanet simulations using the Model for Prediction across Scales-Atmosphere. *Journal of Advances in Modeling Earth Systems*, 12(10), e2020MS002102. https://doi.org/10.1029/2020MS002102
- Rios-Berrios, R., Tang, B. H., Davis, C. A., & Martinez, J. (2024). Modulation of tropical cyclogenesis by convectively coupled kelvin waves. Monthly Weather Review, 152(10), 2309–2322. https://doi.org/10.1175/mwr-d-24-0052.1
- Rossow, W. B., Mekonnen, A., Pearl, C., & Goncalves, W. (2013). Tropical precipitation extremes. *Journal of Climate*, 26(4), 1457–1466. https://doi.org/10.1175/jcli-d-11-00725.1
- Schneider, T., Bischoff, T., & Haug, G. H. (2014). Migrations and dynamics of the Intertropical Convergence Zone. *Nature*, 513(7516), 45–53. https://doi.org/10.1038/nature13636
- Schneider, T., & Walker, C. C. (2006). Self-organization of atmospheric macroturbulence into critical states of weak nonlinear eddy-eddy interactions. *Journal of the Atmospheric Sciences*, 63(6), 1569–1586. https://doi.org/10.1175/jas3699.1
- Schulzweida, U. (2022). CDO user guide. Zenodo. https://doi.org/10.5281/zenodo.7112925
- Segura, H., Pedruzo-Bagazgoitia, X., Weiss, P., Müller, S. K., Rackow, T., Lee, J., et al. (2025). nextGEMS: Entering the era of kilometer-scale Earth system modeling (pp. 1–39). EGUsphere. Retrieved from https://egusphere.copernicus.org/preprints/2025/egusphere-2025-509/doi:10. 5194/egusphere-2025-509

RIOS-BERRIOS ET AL. 24 of 25



# **Journal of Advances in Modeling Earth Systems**

- 10.1029/2025MS005119
- Seidel, D. J., Fu, Q., Randel, W. J., & Reichler, T. J. (2007). Widening of the tropical belt in a changing climate. *Nature Geoscience*, 1(1), 21–24. https://doi.org/10.1038/ngeo.2007.38
- Sherwood, S. C., Bony, S., & Dufresne, J.-L. (2014). Spread in model climate sensitivity traced to atmospheric convective mixing. *Nature*, 505(7481), 37–42. https://doi.org/10.1038/nature12829
- Skamarock, W. C., Klemp, J. B., Duda, M. G., Fowler, L. D., Park, S.-H., & Ringler, T. D. (2012). A multiscale nonhydrostatic atmospheric model using centroidal voronoi tesselations and C-Grid staggering. *Monthly Weather Review*, 140(9), 3090–3105. https://doi.org/10.1175/MWR-D-11-00215.1
- Smagorinsky, J. (1963). General circulation experiments with the primitive equations: I. the basic experiment. *Monthly Weather Review*, 91(3), 99–164. https://doi.org/10.1175/1520-0493(1963)091(0099:gcewtp)2.3.co:2
- Staten, P. W., Grise, K. M., Davis, S. M., Karnauskas, K. B., Waugh, D. W., Maycock, A. C., et al. (2020). Tropical widening: From global variations to regional impacts. Bulletin America Meteorology Social, 101(6), E897–E904. https://doi.org/10.1175/bams-d-19-0047.1
- Staten, P. W., Lu, J., Grise, K. M., Davis, S. M., & Birner, T. (2018). Re-examining tropical expansion. *Nature Climate Change*, 8(9), 768–775. https://doi.org/10.1038/s41558-018-0246-2
- Stevens, B., Satoh, M., Auger, L., Biercamp, J., Bretherton, C. S., Chen, X., et al. (2019). DYAMOND: The DYnamics of the atmospheric general circulation modeled on non-hydrostatic domains. *Progress in Earth and Planetary Science*, 6(1), 61. https://doi.org/10.1186/s40645-019-0304-z
- Sui, C.-H., Li, X., & Yang, M.-J. (2007). On the definition of precipitation efficiency. *Journal of the Atmospheric Sciences*, 64(12), 4506–4513. https://doi.org/10.1175/2007ias2332.1
- Terai, C. R., Keen, N. D., Caldwell, P. M., Beydoun, H., Bogenschutz, P. A., Chao, L.-W., et al. (2025). Climate response to warming in CESS-potter simulations using the global 3-km scream. *Journal of Advances in Modeling Earth Systems, submitted.* https://doi.org/10.22541/essoar. 173655643.33295443/v1
- Thompson, G., Field, P. R., Rasmussen, R. M., & Hall, W. D. (2008). Explicit forecasts of winter precipitation using an improved bulk microphysics scheme. Part II: Implementation of a new snow parameterization. *Monthly Weather Review*, 136(12), 5095–5115. https://doi.org/10.1175/2008MWR2387.1
- Tinney, E. N., Homeyer, C. R., Elizalde, L., Hurst, D. F., Thompson, A. M., Stauffer, R. M., et al. (2022). A modern approach to a stability-based definition of the tropopause. *Monthly Weather Review*. 150(12), 3151–3174. https://doi.org/10.1175/mwr-d-22-0174.1
- Wang, W. (2022). Forecasting convection with a "scale-aware" Tiedtke cumulus parameterization scheme at kilometer scales. Weather and Forecasting, 37(8), 1491–1507. https://doi.org/10.1175/waf-d-21-0179.1
- Webb, M. J., Andrews, T., Bodas-Salcedo, A., Bony, S., Bretherton, C. S., Chadwick, R., et al. (2017). The Cloud Feedback Model Intercomparison Project (CFMIP) contribution to CMIP6. *Geoscientific Model Development*, 10(1), 359–384. https://doi.org/10.5194/gmd-10-359-2017
- Webb, M. J., Lambert, F. H., & Gregory, J. M. (2012). Origins of differences in climate sensitivity, forcing and feedback in climate models. *Climate Dynamics*, 40(3–4), 677–707. https://doi.org/10.1007/s00382-012-1336-x
- Westra, S., Alexander, L. V., & Zwiers, F. W. (2013). Global increasing trends in annual maximum daily precipitation. *Journal of Climate*, 26(11), 3904–3918. https://doi.org/10.1175/jcli-d-12-00502.1
- Wilcox, E. M., & Donner, L. J. (2007). The frequency of extreme rain events in satellite rain-rate estimates and an atmospheric general circulation model. *Journal of Climate*, 20(1), 53–69. https://doi.org/10.1175/jcli3987.1
- Wilson, P. S., & Toumi, R. (2005). A fundamental probability distribution for heavy rainfall. *Geophysical Research Letters*, 32(14), 1–4. https://doi.org/10.1029/2005gl022465
- Xia, Y., Hu, Y., & Liu, J. (2020). Comparison of trends in the Hadley circulation between CMIP6 and CMIP5. Science Bulletin, 65(19), 1667–1674. https://doi.org/10.1016/j.scib.2020.06.011

RIOS-BERRIOS ET AL. 25 of 25